

Real-Space Chemistry on Quantum Computers: A Fault-Tolerant Algorithm with Adaptive Grids and Transcorrelated Extension

César Feniou,^{1, 2,*} Christopher Cherfan,^{2, 3} Julien Zylberman,⁴ Baptiste Claudon,^{5, 1, 2} Jean-Philip Piquemal,^{1, 2, †} and Emmanuel Giner^{1, ‡}

¹*Sorbonne Université, LCT, UMR 7616 CNRS, 75005 Paris, France*

²*Qubit Pharmaceuticals, Advanced Research Department, 75014 Paris, France*

³*École Polytechnique Fédérale de Lausanne (EPFL), 1015 Lausanne, Switzerland*

⁴*Sorbonne Université, Observatoire de Paris, Université PSL, CNRS, LUX, 75005 Paris, France*

⁵*Sorbonne Université, LJLL, UMR 7198 CNRS, 75005 Paris, France*

First-quantized, real-space formulations of quantum chemistry on quantum computers are appealing: qubit count scales logarithmically with spatial resolution, and Coulomb operators achieve quadratic instead of quartic computational scaling of two-electron interactions. However, existing schemes employ uniform discretizations, so the resolution required to capture electron–nuclear cusps in high-density regions oversamples low-density regions, wasting computational resources. We address this by deploying non-uniform, molecule-adaptive grids that concentrate points where electronic density is high. Using Voronoi partitions of these grids, the molecular Hamiltonian is expressed in a Hermitian form and in a transcorrelated, isospectral form that eliminates Coulomb singularities and yields cusp-free eigenfunctions. Both formulations slot naturally into quantum eigenvalue solvers: Hermitian Quantum Phase Estimation (QPE) and the recent generalised Quantum Eigenvalue Estimation (QEVE) protocol for its non-Hermitian, transcorrelated counterpart. Numerical validation on benchmark systems confirms that this non-heuristic ab initio framework offers a promising path for accurate ground-state chemistry on quantum hardware.

I. INTRODUCTION

A. History and Motivation

In 1982, Feynman suggested that quantum computers could efficiently simulate quantum systems [1], launching efforts to build quantum hardware and develop quantum algorithms with the potential to outperform classical methods for specific problems. In that regard, quantum chemistry stands out as a promising application where a true quantum computing advantage could be found since available techniques such as the Quantum Phase Estimation (QPE) intends to provide polynomial cost solutions to the time-independent, non-relativistic Schrödinger equation. Of course, this comes at two conditions: i) to be able to provide an appropriate initial state; ii) to access a fault-tolerant quantum computer (FTQC) to handle the complex quantum circuits [2, 3]. QPE for quantum chemistry was initially developed in the second-quantized framework, where the electronic Hamiltonian is represented on a set of N spinorbitals (*e.g.* Gaussian atom-centered functions). The spectrum can be accessed either by time-evolving the system, originally via Trotterization [4–7], later via Taylorization [8, 9], or by applying a qubitized walk operator [10]. In this setting, the wavefunction requires $\mathcal{O}(N)$ qubits (one per spinorbital), and the gate complexity becomes particularly favorable when the particle number η is in the order of the orbital count [11]. Nevertheless, reaching the typical chemical accuracy, *e.g.* an error of 0.04 eV compared to the exact total energy, requires reaching the complete basis-set (CBS) limit, which in

turn necessitates using far more basis functions than particles ($\eta \ll N$) [12]. In that context, the following first-quantized formalism appears as a preferable scheme due to its low computational scaling in terms of both the number of particles and discretization points. In this *first-quantised* picture, each of the η electrons has its own register that stores the binary index of a grid point among the N available sites. Indexing N sites requires only $\lceil \log_2 N \rceil$ qubits, so the complete η -electron configuration space fits in $\eta \lceil \log_2 N \rceil = \mathcal{O}(\eta \log N)$ qubits. Fermionic antisymmetry is enforced by projecting onto the subspace that is antisymmetric under exchange of these registers, as detailed in Ref. [13]. However, since standard overlapping integrals introduce $\mathcal{O}(N^4)$ two-body terms, the gate complexity is driven to similarly high powers of N , negating much of the practical advantage over second quantization. To address this, alternative discretization schemes have been developed with the goal of preserving a diagonal structure for the two-body operator in real space, thus reducing the Hamiltonian term count to $\mathcal{O}(N^2)$. Examples include uniform real-space grids [14–16], gausslets and mostly planewaves [13, 17–20], and led to overall QPE gate complexities as small as $\mathcal{O}(\eta^{8/3} N^{1/3} \epsilon^{-1})$ using on-the-fly Hamiltonian term computation [13, 18]. Although asymptotically appealing, these discretisation schemes impose *uniform spatial resolution*, which is particularly ill-suited to capture sharp features, known as cusps, that appear in the wavefunction near Coulomb singularities (*e.g.* where particles coincide) [21], since the fine resolution required near nuclei would simultaneously oversample low-density regions, leading to a large computational overhead. Moreover, accurate resolution of cusps inherently amplifies the spectral norms, since it explores near-singularity regions and thus correspondingly raises the total QPE complexity.

As a result, and despite new trade-offs and promising asymptotics, quantum computing still faces the age-

* cesarf@qubit-pharmaceuticals.com

† jean-philip.piquemal@sorbonne-universite.fr

‡ emmanuel.giner@lct.jussieu.fr

old challenge of resolving electronic wavefunction cusps without incurring prohibitive computational cost [12, 15, 22].

In this work, we present a new framework for improved spatial accuracy in a real-space, first-quantized setting. The first strategy uses adaptive multicenter grids, rooted in Density Functional Theory (DFT) integration techniques [23, 24], to concentrate points in regions of high electron density, and implements the Laplacian via a Voronoi-based finite-volume scheme [25–27]. We derive a Hermitian Hamiltonian in this basis and outline its integration into a qubitized-QPE protocol. The second strategy uses a similarity transformation to produce the *transcorrelated* (TC) Hamiltonian [28], which is isospectral to the original but replaces Coulomb singularities with finite effective interactions. The TC Hamiltonian eigenstates are free of electron–nucleus and electron–electron cusps, eliminating the need for excessively tight grids. On the drawback side, the TC Hamiltonian exhibits a three-body operator, and non-Hermitian terms, turning the Schrödinger eigenvalue problem into a non-self-adjoint (generalized) eigenvalue problem. Thus, the usual QPE algorithm becomes inapplicable. Though, recent advances in eigenvalue processing have introduced *Quantum EigenValue Estimation* (QEVE) algorithms [29], that enables efficient eigenvalue estimation for non-Hermitian matrices. Building upon this, we derive a TC Hamiltonian in the adaptive grid basis, and outline its integration into a QEVE protocol.

For each approach, we provide a detailed methodology and support its robustness with numerical simulations, while noting that the scheme offers numerous opportunities for improvement.

B. Problem Statement

This study addresses the central challenge of quantum chemistry: describing molecular electronic structure and properties through the non-relativistic, time-independent Schrödinger equation. This equation describes the η electrons, located at positions $\{\mathbf{x}_i\}_{i=0}^{\eta-1} \subset \mathbb{R}^3$, which interact among themselves through a repulsive Coulomb potential and with the M nuclei with respective charges $\{\mathcal{Z}_\alpha\}_{\alpha=0}^{M-1}$ through an attractive Coulomb potential. As usual in quantum chemistry, we employ the Born–Oppenheimer approximation [30] which leads to clamped nuclei, *i.e.* the positions of the nuclei $\{\mathbf{R}_\alpha\}_{\alpha=0}^{M-1}$ are considered fixed. Therefore, within the Born–Oppenheimer approximation, the total molecular Schrödinger equation is written as

$$\hat{H}\Psi(\mathbf{x}_0, \dots, \mathbf{x}_{\eta-1}) = E\Psi(\mathbf{x}_0, \dots, \mathbf{x}_{\eta-1}), \quad (1)$$

where the Hamiltonian \hat{H} is given, in atomic units, by

$$\hat{H} = \sum_{i=0}^{\eta-1} \left(-\frac{1}{2} \nabla_{\mathbf{x}_i}^2 - \sum_{\alpha=0}^{M-1} \frac{\mathcal{Z}_\alpha}{|\mathbf{x}_i - \mathbf{R}_\alpha|} + \sum_{j>i}^{\eta-1} \frac{1}{|\mathbf{x}_i - \mathbf{x}_j|} \right). \quad (2)$$

In Eq. (1), the wave function $\Psi(\mathbf{x}_0, \dots, \mathbf{x}_{\eta-1})$ corresponds to the i -th eigenstate of the Hamiltonian,

and as any fermionic wave function, is antisymmetric with respect to exchange of any couple of particles, *i.e.*

$$\Psi(\dots, \mathbf{x}_i, \dots, \mathbf{x}_j, \dots) = -\Psi(\dots, \mathbf{x}_j, \dots, \mathbf{x}_i, \dots) \quad \forall i, j, \quad (3)$$

with $|\Psi_i|^2$ representing the probability density for the electron’s positions in the i -th eigenstate. The real number E_i in Eq. (1) is the total energy of the system associated to the i -th eigenstate, which is the central quantity needed to compute many physico-chemical properties in molecular systems. Among all eigenvalues of the Hamiltonian, the lowest one E_0 plays a special role, and can be recast as the solution of the following minimization problem

$$E_{GS}^* = \min_{\Psi \in \mathcal{H}_{as}^1(\mathbb{R}^{3\eta})} \frac{\int \Psi^* \hat{H} \Psi \prod_{i=0}^{\eta-1} d\mathbf{x}_i}{\int |\Psi|^2 \prod_{i=0}^{\eta-1} d\mathbf{x}_i}, \quad (4)$$

where $\mathcal{H}_{as}^1(\mathbb{R}^{3\eta})$ is the space of antisymmetric, square-integrable functions of 3η variables with finite kinetic energy. On classical computers, determining the energy of the ground state within chemical accuracy (*i.e.* within an error of 0.0016 a.u. or equivalently 0.04 eV) exhibits exponential complexity with the size of the problem (space dimension and number of particles) [31].

C. First-Quantized Molecular Simulation via Qubitized QPE

This section reviews the qubitized-QPE procedure for ground-state energy estimation of first-quantized molecular Hamiltonians, and gives a qualitative and intuitive explanations of the leading order scaling complexities. Consider the above electronic system of η electrons, each described in a spatial discretization basis of N elements. In the first-quantization formalism, each electron is encoded in a quantum register of $\log N$ qubits, and the η -electron wavefunction is obtained by tensor multiplying single-electron states. The number of qubits to encode this wave function scales therefore as $\mathcal{O}(\eta \log N)$. Since the fermionic antisymmetry is not embedded in the Hamiltonian, it must therefore be enforced directly on the wavefunction, a process that can be performed with negligible additional gate complexity $\mathcal{O}(\eta \log \eta \log N)$ [32]. The first quantized Hamiltonian, once discretized on a chosen spatial basis, is usually expressed as a linear combination of unitaries (LCU). From this decomposition one constructs the corresponding qubitized quantum-walk operator, unitary and spectrum-related to the original Hamiltonian, whose eigenvalues can then be extracted using the QPE algorithm [10]. This now usual protocol is outlined more precisely in Appendix D. Phase estimation then uses $\tilde{\mathcal{O}}(C_H \lambda \epsilon^{-1})$ logical gates, where ϵ is the target energy error, C_H is the cost of block-encoding the walk operator, λ is the one-norm of the LCU of the Hamiltonian matrix as defined in D2, and $\tilde{\mathcal{O}}$ hides poly-logarithmic factors [10]. C_H has been shown to scale as $\tilde{\mathcal{O}}(\eta)$ [9]. The

LCU norm is fundamentally governed by the *minimal spatial separation* between electrons (as $\mathcal{O}(\eta/(\Delta r)^2)$ for the kinetic part and $\mathcal{O}(\eta^2/\Delta r)$ for the Coulomb part). For a uniform lattice or plane-wave grid the spacing scales as $\Delta r \sim (\Omega/N)^{1/3}$ with volume $\Omega \propto \eta$. Consequently, the one-norm of the LCU of the kinetic and potential operator are $\lambda_T = \mathcal{O}(\eta^{1/3} N^{2/3})$ and $\lambda_V = \mathcal{O}(\eta^{5/3} N^{1/3})$ respectively, so $\lambda = \mathcal{O}(\eta^{4/3} N^{2/3} + \eta^{8/3} N^{1/3})$, yielding a total baseline scaling of $\tilde{\mathcal{O}}((\eta^{4/3} N^{2/3} + \eta^{8/3} N^{1/3}) \epsilon^{-1})$ first given in [9, 13]. Notice that for systems where the first term dominates, it has been proposed to compute the kinetic operator *on the fly* in the momentum basis within the interaction picture, thus avoiding incurring the cost associated with the λ_T value of the kinetic operator as usually done using LCU. The QPE cost following this technique was shown to be reduced to $\mathcal{O}(\eta^{8/3} N^{1/3} \epsilon^{-1})$ [18]. Plane-wave bases, though ideal for periodic solids, are poorly suited to chemistry and strongly correlated systems: their uniform spatial resolution forces massive oversampling of low-density regions just to resolve core cusps and valence oscillations, leading to a significant computational overhead. In practice, plane waves are always used in combination with pseudopotentials [21], which simplify the treatment of core regions by approximating core electrons as frozen and replacing their interactions with an effective external potential. Well aware of this, the embedding of pseudopotentials to quantum simulation using planewaves has been proposed and quantified [19]. Nevertheless, the non locality of the pseudo potentials induces computational overheads or localization approximations, as usual in real-space calculations.

II. SPACE DISCRETISATION TAILORED TO MOLECULAR SYSTEMS

A. Multi-center Molecular Grids

In real-space grid methods, accurately resolving the Coulomb singularity requires local refinement near the nuclei. A natural strategy to increase point density in these regions is to construct a union of spherical grids centered around each nucleus, using a radial discretization that becomes progressively more concentrated near its center. Such discretizations have been extensively explored and optimized in the context of density functional theory (DFT), as they are commonly used for evaluating energy functionals via numerical integration over space. The radial discretization often follows a Becke scheme [33] which can be summarized as follows. Given a uniform partition u_i of the interval $[0; 1]$, the radial coordinate is discretized into N_r points according to

$$r_i = -\alpha \ln(1 - u_i^\nu), \quad (5)$$

where α and $\nu > 0$ control both the overall range and the concentration of points around the origin. For the angular component, several options are available. One possibility is to use Gauss-Legendre quadratures [34] such

that the angular points are discretized into respectively N_θ and N_ϕ grid points $\theta_j \in [0; \pi]$ and $\phi_k \in [0; 2\pi]$ via

$$\begin{cases} \theta_j = \frac{\pi}{2}(x_j + 1) \\ \phi_k = \delta k, \end{cases} \quad (6)$$

where x_j is the j th root of the Legendre polynomial of degree N_θ (in ascending order), and the azimuthal angle repartition is uniform with constant step size δ . Since the θ and ϕ partitions are built independently, every node has natural neighbors in r , θ , and ϕ , which simplifies finite-difference derivative approximations. However, as can be seen from Fig. 1a, we illustrated the various schemes by representing the real-space grids obtained for the H₂O molecule, the Gauss-Legendre quadrature exhibits a dense clustering of points along lines of latitude close to the north and south poles of each sphere, thus breaking rotational symmetry. An alternative and potentially more adequate approach is to use the so-called Lebedev angular quadrature, which is widely adopted for accurate multi-center numerical integration schemes, among which those used for routine DFT calculations in molecular systems. It is based on a class of quadratures that are invariant around the octahedral point group, by solving non-linear equations that ensure invariant spherical harmonics [35]. An illustrative example of a multicenter molecular grid combining Becke radial discretisation and Lebedev quadrature is shown in Fig. 1b. From the latter plot, it clearly appears that, with respect to the grids based on the Gauss-Legendre angular discretization, the grids based on the Lebedev angular discretization are closer to the local rotational symmetry.

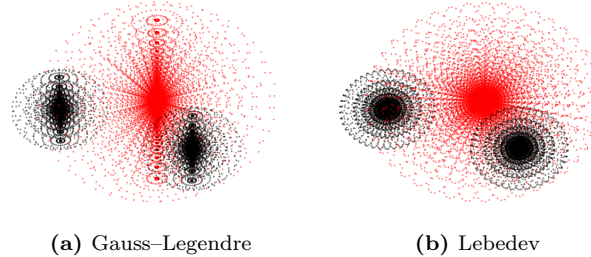


FIG. 1: Visualization, in the case of a water molecule, of the two types of spatial discretizations used here, *i.e.* Gauss-Legendre and Lebedev. Atomic distances are not at scale for clarity, and colors are only illustrative.

B. Voronoi Finite Volume Discretization

Although a finite-difference scheme might seem a natural choice on the grid described above, there are disadvantages in doing so: (i) the presence of multiple grids makes it ambiguous to define nearest neighbors for a given coordinate, especially if the grids are overlapping and (ii) there is no simple linear relation between the Laplacian in a grid centered at the origin $\nabla_{\mathbf{x}_i}^2$, and the Laplacian on a grid shifted to \mathbf{R}_α , *i.e.* $\nabla_{\mathbf{x}_i - \mathbf{R}_\alpha}^2$. To avoid these issues, and without imposing any restrictions on the underlying grid, we adopt a finite-volume approach using Voronoi cells. This scheme has previously been used

to classically solve the transport-diffusion equations [36, 37], and has been used by [25] to solve the molecular Schrödinger equation using similar molecular multicenter grids. We briefly report here the main concepts used for our present approach.

1. Voronoi Diagrams

Definition II.1 (Voronoi Cells and Diagram). Given a set \mathcal{V} of N arbitrarily distributed points $\{\mathbf{r}_m\}_{m=0}^{N-1} \subset \mathbb{R}^3$, the Voronoi cell $\text{Vor}(\mathbf{r}_m)$ associated with point \mathbf{r}_m is defined as the region of space closer to \mathbf{r}_m than to any other point. In mathematical terms:

$$\text{Vor}(\mathbf{r}_m) = \left\{ \mathbf{r} \in \mathbb{R}^3 : \|\mathbf{r} - \mathbf{r}_m\| \leq \|\mathbf{r} - \mathbf{r}_n\| \quad \forall m \neq n \right\}. \quad (7)$$

The Voronoi diagram of \mathcal{V} is then the union of all Voronoi cells in \mathcal{V} :

$$\text{Vor}(\mathcal{V}) = \bigcup_{m=0}^{N-1} \text{Vor}(\mathbf{r}_m). \quad (8)$$

Note that the definition could be formulated for points in higher dimensions and for metrics other than the Euclidean one. This partitioning yields a unique Voronoi diagram, in which the space is discretized into convex polyhedral cells [38].

Definition II.2 (Natural Neighbors and Voronoi Facets). Given a set \mathcal{V} of N arbitrarily distributed points $\{\mathbf{r}_m\}_{m=0}^{N-1} \subset \mathbb{R}^3$, a point \mathbf{r}_n is called a natural neighbor of \mathbf{r}_m if and only if

$$\Gamma_{mn} := \text{Vor}(\mathbf{r}_m) \cap \text{Vor}(\mathbf{r}_n) \neq \emptyset. \quad (9)$$

We denote by $\Lambda(m)$ the set of indices of the natural neighbors of \mathbf{r}_m , *ie*

$$\Lambda(m) = \{n : \Gamma_{mn} \neq \emptyset\}, \quad (10)$$

and we call Γ_{mn} , the intersection of the Voronoi cells of two natural neighbors \mathbf{r}_m and \mathbf{r}_n , a Voronoi facet.

By construction, Γ_{mn} lies on the perpendicular bisector of the segment connecting these two points. In 3D, its area σ_{mn} can be calculated from its surrounding vertices $\{\xi_k\}$ via

$$\sigma_{mn} = \frac{1}{2} \sum_{k=0}^{\Xi-1} \|(\xi_k - \rho_{mn}) \times (\xi_{k+1} - \rho_{mn})\|, \quad (11)$$

where $\rho_{mn} = (\mathbf{r}_m + \mathbf{r}_n)/2$, and Ξ is the number of surrounding vertices, with $\xi_{M+1} = \xi_1$. The cell $\text{Vor}(\mathbf{r}_m)$ has a volume v_m that can be expressed as the sum of the volumes of pyramids with base of area σ_{mn} and apex at \mathbf{r}_m :

$$v_m = \frac{1}{6} \sum_{n \in \Lambda(m)} |\mathbf{r}_m - \mathbf{r}_n| \sigma_{mn}. \quad (12)$$

There exists many algorithms that provide the Voronoi diagrams of a given set of points, *ie* the location of

the vertices of each Voronoi facet with their areas and the volume of each Voronoi cell [39, 40]. Although their time complexity in worse-case scenarios could scale superpolynomially, in practice and for well-structured sets of points, the Voronoi diagram can be computed in polynomial time [41]. As an illustration, we display in figure 2 the Voronoi diagram generated by the *Qhull* library [42] for a set of points in 2D.

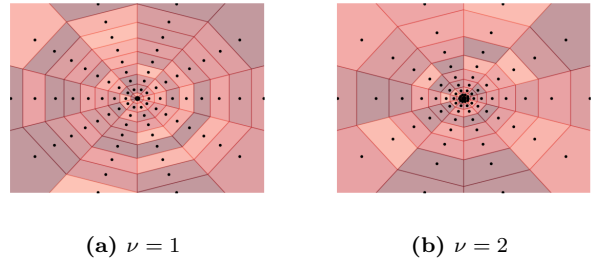


FIG. 2: Voronoi diagram for a set of planar points following a Becke radial discretization (5) and a uniform angular partition. The Voronoi cells of each black dot are delimited with random shades of red.

C. Wavefunction Representation

Let us now address the problem of the representation of the wave function on the grids previously introduced. Consider a single electron wavefunction discretized on a multi-center grid with N points. It can be encoded in a $\log(N)$ -qubit register as

$$|\psi_e\rangle = \sum_{m=0}^{N-1} c_m |m\rangle, \quad (13)$$

where m runs through the indices of the cells in the Voronoi diagram. The state (13) resides in the N -dimensional Hilbert space \mathcal{H}_e and the expansion coefficients c_m satisfy the usual orthonormality condition $\sum_{m=0}^{N-1} |c_m|^2 = 1$, provided that $\langle m' | m \rangle = \delta_{mm'}$. For an η -electron system, the wavefunction is represented by a quantum register formed from the tensor product of η single-electron wavefunctions. The total state vector thus lives in $\mathcal{H}_{\text{tot}} = \bigotimes_{i=1}^{\eta} \mathcal{H}_e$, and can be encoded using $\eta \log(N)$ qubits. Electrons being fermions, the electronic wavefunction must live in the antisymmetric subspace of \mathcal{H}_{tot} , which we ensure using the gate anti-symmetrization gate described in [32].

1. Finite Volume Scheme

We now give the matrix representation of the molecular Hamiltonian in the discretized space of the grid points. The mathematical derivation of the finite volume scheme is presented in Appendix A. The main idea is to integrate the molecular Schrödinger equation over the volumes of the Voronoi cells occupied by each electron, and take the average in the limit of infinitesimally small Voronoi cell volumes so as to express volume and surface integrals

in terms of the parameters of the Voronoi diagrams. Scalar operators, like the Coulombic potential terms, are represented as diagonal matrices with each diagonal elements being the value of the operator evaluated for the corresponding grid point. Ultimately, finding the ground-state energy boils down to find the smallest eigenvalue of the finite volume discretized Hamiltonian, which can be represented in matrix form as

$$\begin{aligned} \mathbf{H} = & \sum_{i=0}^{\eta-1} \left(-\frac{1}{2} \sum_{m,n=0}^{N-1} \mathbf{L}_{mn} |m\rangle_i \langle n|_i - \sum_{m=0}^{N-1} \mathbf{U}_m |m\rangle_i \langle m|_i \right) \\ & + \sum_{i=0}^{\eta-1} \sum_{j>i} \sum_{m,p=0}^{N-1} \mathbf{W}_{mp} |m\rangle_i \langle m|_i |p\rangle_j \langle p|_j, \end{aligned} \quad (14)$$

where the discretized Laplacian matrix has matrix elements

$$\mathbf{L}_{mn} = \begin{cases} -\frac{1}{v_m} \sum_{k \in \Lambda(m)} \frac{\sigma_{mk}}{|\mathbf{r}_m - \mathbf{r}_k|} & \text{if } m = n, \\ \frac{1}{v_m} \frac{\sigma_{mn}}{|\mathbf{r}_m - \mathbf{r}_n|} & \text{if } n \in \Lambda(m), \\ 0 & \text{otherwise,} \end{cases} \quad (15)$$

with v_m and σ_{mn} defined in Eqs. (11) and (12), the Coulombic electron-nuclei attraction operator is diagonal in the position basis, with the following elements:

$$\mathbf{U}_m = \sum_{\alpha=0}^{M-1} \frac{\mathcal{Z}_\alpha}{|\mathbf{r}_m - \mathbf{R}_\alpha|}, \quad (16)$$

and the two-body electron-electron Coulomb repulsion operator is diagonal in the tensor-product position basis:

$$\mathbf{W}_{mp} = \frac{1}{|\mathbf{r}_m - \mathbf{r}_p|}. \quad (17)$$

The notation $|m\rangle_i \langle n|_i$ refers to the outer product $|m\rangle \langle n|$ in the space of the i th electron. More precisely:

$$\begin{aligned} |m\rangle_i \langle n|_i &= \underbrace{\mathbf{I}_N \otimes \cdots \otimes \mathbf{I}_N}_{i\text{-times}} \otimes |m\rangle \langle n| \otimes \underbrace{\mathbf{I}_N \otimes \cdots \otimes \mathbf{I}_N}_{(\eta-i+1)\text{-times}} \\ &= \mathbf{I}_{N^i} \otimes |m\rangle \langle n| \otimes \mathbf{I}_{N^{\eta-i+1}} \end{aligned} \quad (18)$$

The representation of the molecular Hamiltonian on a multi-center grid being rather unusual for the quantum chemistry community, it naturally calls some remarks regarding important numerical features such as convergence, sparsity and hermiticity. Firstly, finding the error associated to approximating an infinitesimal volume to the volume of a Voronoi cell is a complex problem-specific task, which we will not delve into. However, one can justify the convergence of the problem of finding ground state using this framework by considering the Schrödinger equation in imaginary time as a diffusion equation, whose Voronoi finite volume scheme was proven to be convergent [36, 37]. Furthermore, in fixed-dimensional space, the Voronoi

Laplacian is sparse, where the m -th row contains $|\Lambda(m)|+1$ non-zero entries (one per neighbor and itself). This sparsity reflects the local connectivity of the Voronoi mesh, and does not scale with the total number of discretization points. Last but not least, due to the non-uniform grid spacing and the corresponding variation in Voronoi cell volumes, the discretized Laplacian does not have a Hermitian matrix representation. However, there is an easy way to symmetrize equation (15) and re-obtain an Hermitian Hamiltonian, as it is done in Ref. 27. In the latter scheme, the diagonal potential energy matrix remains intact while the modified Laplacian matrix, denoted by $\bar{\mathbf{L}}_{mn}$, has elements given by

$$\bar{\mathbf{L}}_{mn} = \sqrt{\frac{v_m}{v_n}} \mathbf{L}_{mn}. \quad (19)$$

III. HERMITIAN HAMILTONIAN BLOCK-ENCODING FOR QPE

Considering a molecular system described in first quantization by the Hamiltonian of Eq. (2), its symmetrized representation in the grid position basis of N points is then naturally rewritten as the sum of a one-body and two-body operators

$$\begin{aligned} \bar{\mathbf{H}} = & \sum_{m,n=0}^{N-1} \bar{\mathbf{T}}_{mn} \sum_{i=0}^{\eta-1} |m\rangle_i \langle n|_i \\ & + \sum_{m,p=0}^{N-1} \mathbf{W}_{mp} \sum_{j>i}^{\eta-1} |m\rangle_i \langle m|_i |p\rangle_j \langle p|_j, \end{aligned} \quad (20)$$

where \mathbf{W}_{mp} is defined in equation (17) and

$$\bar{\mathbf{T}}_{mn} = -\frac{1}{2} \bar{\mathbf{L}}_{mn} - \begin{cases} \mathbf{U}_m & \text{if } m = n, \\ 0 & \text{otherwise,} \end{cases} \quad (21)$$

and where $\bar{\mathbf{L}}_{mn}$ are the symmetrized matrix elements defined in Eq. (19), and \mathbf{U}_m defined in Eq. (16).

The block encoding can then be constructed using the systematic Pauli LCU decomposition in the first quantization, as introduced in [20, 43], and is valid for arbitrary basis sets, including one that diagonalizes the potential energy. We quote the expression in [20] for the Pauli LCU decomposition of a Hamiltonian that can be decomposed into a one-body term and a diagonal two-body term:

$$\begin{aligned} \bar{\mathbf{H}} = & \sum_{m,n=0}^{N-1} \omega_{mn} \sum_{i=0}^{\eta-1} \prod_{b=0}^{\log N-1} \mathbf{X}_{i \log N+b}^{m_b} \mathbf{Z}_{i \log N+b}^{n_b} \\ & + \frac{1}{2} \sum_{m,p=0}^{N-1} \gamma_{mp} \sum_{i \neq j}^{\eta-1} \prod_{b=0}^{\log N-1} \mathbf{Z}_{i \log N+b}^{m_b} \mathbf{Z}_{j \log N+b}^{p_b}, \end{aligned} \quad (22)$$

where m_b is the b -th bit in the binary representation of m , likewise for n_b and p_b , and \mathbf{X}_i and \mathbf{Z}_i are Pauli operators acting on the i -th qubit:

$$\begin{aligned} \mathbf{X}_i &= \mathbf{I}_{2^i} \otimes \mathbf{X} \otimes \mathbf{I}_{2^{\eta \log N - i - 1}} \\ \mathbf{Z}_i &= \mathbf{I}_{2^i} \otimes \mathbf{Z} \otimes \mathbf{I}_{2^{\eta \log N - i - 1}}. \end{aligned} \quad (23)$$

The explicit expressions of the coefficients are

$$\omega_{mn} = \frac{1}{N} \sum_{x=0}^{N-1} (-1)^{x \odot n} \bar{\mathbf{T}}_{m \oplus x, x}, \quad (24)$$

$$\gamma'_{mp} = \frac{1}{N^2} \sum_{x,y=0}^{N-1} (-1)^{(m \odot x) + (y \odot p)} \mathbf{W}_{xy}. \quad (25)$$

In Eqs. (24) and (25), \oplus is the bitwise XOR operation and \odot is the bitwise dot product. The expressions of $\bar{\mathbf{T}}_{mn}$ and \mathbf{W}_{mp} are given by equations (21), (16) and (17). One can reduce the number of coefficients to load by neglecting terms with identity Pauli strings, since they only contribute to a constant shift of the eigenvalue. This is done by not considering coefficients for which both indices are zero. Also, one can incorporate repeating strings in the one-body and two-body terms into a single coefficient, which corresponds to that of the string containing a \mathbf{Z} gate on only one of the qubits. Noticing that $\gamma'_{mp} = \gamma'_{pm}$, we can rewrite the LCU decomposition of the Hamiltonian with these modifications:

$$\begin{aligned} \bar{\mathbf{H}}_{LCU} = & \sum_{m,n=0}^{N-1} \omega'_{mn} \sum_{i=0}^{\eta-1} \prod_{b=0}^{\log N-1} \mathbf{X}_{i \log N+b}^{m_b} \mathbf{Z}_{i \log N+b}^{n_b} \\ & + \frac{1}{2} \sum_{m,p=1}^{N-1} \gamma'_{mp} \sum_{i \neq j}^{\eta-1} \prod_{b=0}^{\log N-1} \mathbf{Z}_{i \log N+b}^{m_b} \mathbf{Z}_{j \log N+b}^{p_b}, \end{aligned} \quad (26)$$

where

$$\omega'_{mn} = \begin{cases} 0 & \text{if } m = n = 0, \\ \omega_{0n} + (N-1)\gamma_{0n} & \text{if } m = 0, n \neq 0, \\ \omega_{mn} & \text{otherwise,} \end{cases} \quad (27)$$

$$\gamma'_{mp} = \begin{cases} 0 & \text{if } m = 0 \text{ or } p = 0, \\ \gamma_{mp} & \text{otherwise.} \end{cases} \quad (28)$$

The subscript LCU is added to differentiate between the true Hamiltonian and the one without identity strings.

IV. TRANSCORRELATED MOLECULAR HAMILTONIAN

Using a physically-relevant grid surely allows to accurately sample the high density regions, but exploring the regions near the cusps of the wave function inherently increases the norms of the operators, and thus the associated QPE complexity. The latter can be qualitatively understood by noticing that the Coulomb potential diverges at coalescence, and the norm of the Laplacian grows quadratically as the resolution increases (see (15)). In this section, we explore the use of a *transcorrelated* (TC) Hamiltonian [28] in order to alleviate the problems inherent to quantum mechanics with Coulomb divergences. This approach

applies an isospectral similarity transformation by a so-called correlation factor, which when properly chosen replaces unbounded Coulomb potentials with non-diverging interactions, to the price of introducing non-Hermitian differential terms together with a three-body interaction. The use of a TC Hamiltonian has multiple consequences which are important to highlight in the present context. Provided that the cusps conditions are included in the correlation factor itself, the effective interactions produced by the similarity transformation are non divergent [28, 44–46], and therefore the TC eigenfunctions are free of cusps. The latter point is crucial in the present context as it prevents the need for extremely dense grid points near the nuclei, and therefore reduces the operator norm of the Laplacian. As mentioned above, the TC Hamiltonian exhibits a three-body interaction, thus increasing the complexity with the number of particles η , which nevertheless remains diagonal and bounded on the basis of the real-space grid and contributes only a constant offset to the operator norm. A crucial aspect in the context of quantum-based algorithm arises from the non-Hermitian differential terms in the TC Hamiltonian, which prevent the use of qubitized QPE. To alleviate this problem, we instead propose to use the recently developed Quantum EigenValue Estimation (QEVE) algorithms, which efficiently handle non-Hermitian operators [29]. Appendix E explicitly outlines the QEVE algorithm, which, like qubitized QPE, relies on block-encoding the non-Hermitian Hamiltonian. Below, we detail the full workflow: deriving the transcorrelated Hamiltonian and its discretized form on the adaptive grid, building the Pauli-LCU decomposition for QEVE compatibility, and validating the approach with numerical simulations of helium atom and hydrogen molecules.

A. Molecular Transcorrelated Hamiltonian in First Quantization

In this section, we briefly introduce the transcorrelated molecular Hamiltonian and its main features. Given a symmetrical function of the η -electron coordinates, labelled here $\tau(\{\mathbf{x}_i\})$, the transcorrelated Hamiltonian is then obtained by a similarity transformation of \hat{H} by e^τ , *i.e.*

$$\tilde{H} := e^{-\tau} \hat{H} e^\tau = \hat{H} + [\hat{H}, \tau] + \frac{1}{2} [[\hat{H}, \tau], \tau]. \quad (29)$$

This equality is obtained from the Baker–Campbell–Hausdorff formula, which in the case of the TC Hamiltonian truncates at second-order, as the fundamental commutator $[\hat{H}, \tau]$ involves a function and a second-order differential operator. This effective Hamiltonian introduces additional potential terms which modify the bare Coulomb interaction, and a non-hermitian first-order differential operator. Nonetheless, as any similarity transformation, it preserves the spectrum of the original operator, here the molecular Hamiltonian \hat{H} . Given parameters

$\mu_{ne}, \mu_{ee} \in \mathbb{R}^+$, and a function

$$\tau(\{\mathbf{x}_i\}) = \sum_{i=0}^{\eta-1} \left(\sum_{\alpha=0}^{M-1} g_{\mu_{ne}}(x_{i\alpha}) + \sum_{j>i}^{n-1} h_{\mu_{ee}}(x_{ij}) \right) \quad (30)$$

where $g_{\mu_{ne}}$ and $h_{\mu_{ee}}$ are respectively functions of the electron-nuclei and electron-electron distances $x_{i\alpha} = |\mathbf{x}_i - \mathbf{R}_\alpha|$ and $x_{ij} = |\mathbf{x}_i - \mathbf{x}_j|$, the similarity-transformed (TC) Hamiltonian \tilde{H} can be written as

$$\begin{aligned} \tilde{H} = & \hat{H} - \sum_{i,\alpha} \tilde{\mathcal{K}}[g_{\mu_{ne}}](\mathbf{x}_i, \mathbf{R}_\alpha) - \sum_{i,\alpha<\beta} \tilde{\mathcal{B}}[g_{\mu_{ne}}](\mathbf{x}_i, \mathbf{R}_\alpha, \mathbf{R}_\beta) \\ & - \sum_{i<j} \tilde{\mathcal{K}}[h_{\mu_{ee}}](\mathbf{x}_i, \mathbf{x}_j) - \sum_{i<j<k} \tilde{\mathcal{B}}[h_{\mu_{ee}}](\mathbf{x}_i, \mathbf{x}_j, \mathbf{x}_k) \end{aligned} \quad (31)$$

where the effective two- and three-body electron-electron operators read

$$\begin{aligned} \tilde{\mathcal{K}}[h_{\mu_{ee}}](\mathbf{x}_i, \mathbf{x}_j) = & \frac{1}{2} \left[\nabla_i^2 h + \nabla_j^2 h + (\nabla_i h)^2 + (\nabla_j h)^2 \right] \\ & + \nabla_i h \cdot \nabla_i + \nabla_j h \cdot \nabla_j \end{aligned} \quad (32)$$

$$\begin{aligned} \tilde{\mathcal{B}}[h_{\mu_{ee}}](\mathbf{x}_i, \mathbf{x}_j, \mathbf{x}_k) = & \nabla_i h_{ij} \cdot \nabla_i h_{ik} + \nabla_j h_{ji} \cdot \nabla_j h_{jk} \\ & + \nabla_k h_{ki} \cdot \nabla_k h_{kj} \end{aligned} \quad (33)$$

with $h \equiv h_{\mu_{ee}}$, $h_{ij} = h(\mathbf{x}_i, \mathbf{x}_j)$ and $\nabla_i \equiv \nabla_{\mathbf{x}_i}$. Similar expressions can analogously be easily written for the nucleus-electron operators $\tilde{\mathcal{K}}[g_{\mu_{ne}}]$ and $\tilde{\mathcal{B}}[g_{\mu_{ne}}]$. An important feature is that, as in practical calculations the operator is discretized in a finite basis set, the original spectrum of \hat{H} is only recovered in the limit of a complete basis set. The advantage of the transcorrelation formalism relies therefore on the fact that if some physics is encoded in τ , the convergence of the low-lying spectrum of the discretized transcorrelated Hamiltonian \tilde{H} is faster than that of the discretized bare Hamiltonian \hat{H} . For instance, if the cusps conditions [47] are encoded within τ , the right-eigenfunctions of \tilde{H} are cusp-free, which suggests a faster convergence when expanded on a finite basis set. There exists therefore a wide variety of functional forms for this correlation factor τ which are all built in terms of the so-called one-, two- and three-body functions which depend on the electron-nuclei, electron-electron and electron-electron-nuclei coordinates, respectively. In this work, we choose the functions $g_{\mu_{ne}}$ and $h_{\mu_{ee}}$ in equation (30) to be

$$g_{\mu_{ne}}(x_{i\alpha}) = x_{i\alpha} (\text{erf}(\mu_{ne} x_{i\alpha}) - Z_\alpha) + \frac{1}{\mu_{ne} \sqrt{\pi}} e^{-(\mu_{ne} x_{i\alpha})^2}, \quad (34)$$

$$h_{\mu_{ee}}(x_{ij}) = x_{ij} (1 - \text{erf}(\mu_{ee} x_{ij})) - \frac{1}{\mu_{ee} \sqrt{\pi}} e^{-(\mu_{ee} x_{ij})^2}. \quad (35)$$

as it is done in the work of [46]. The form of the functions in Eqs. (34) and (35) are such that they reproduce, at leading order in $1/x$, an effective smooth interaction instead of the bare diverging Coulombic interaction (see Ref. 46 for more details). As the parameters μ_{ne} and μ_{ee}

decrease, the effect of the correlation factor τ becomes more important.

B. Transcorrelated Hamiltonian Block Encoding

As the transcorrelated Hamiltonian matrix $\tilde{\mathbf{H}} \in \mathbb{R}^{N^n \times N^n}$ is non-Hermitian matrix, finding its eigenvalues with a quantum algorithm can no longer be accessed through the usual qubitzed QPE procedure. Hence, one needs to consider a larger class of QEVE algorithms. Given an v qubit register, a state $|\psi\rangle \in \mathbb{C}^{N^n}$ that is prepared close to the ground state of $\tilde{\mathbf{H}}$, and a subnormalization constant $\alpha_{\tilde{\mathbf{H}}}$ of $\tilde{\mathbf{H}}$, previous approaches were based on generating (up to a normalization constant) the state [48, 49]

$$\sum_{\ell=0}^{v-1} |\ell\rangle e^{2\pi i \ell \frac{\tilde{\mathbf{H}}}{\alpha_{\tilde{\mathbf{H}}}}} |\psi\rangle \quad (36)$$

and measuring the eigenvalue from the phase that is kick-backed onto the ancilla qubits. However, this algorithm suffers from a suboptimal $\mathcal{O}(\epsilon^{-1} \cdot \text{polylog}(\epsilon^{-1}))$ query complexity dependence on ϵ . To resolve this, [29] introduced an alternative QEVE algorithm based on generating *Chebyshev history states*, and whose query complexity regains the $\mathcal{O}(1/\epsilon)$ of QPE. We summarize this *Quantum Chebyshev Phase Estimation* (QCPE) algorithm in Appendix E and we state the main theorem here.

Theorem IV.1 (Quantum Chebyshev Phase Estimation [29]). Let \mathbf{H} be a square matrix with only real eigenvalues such that \mathbf{H}/α_H is a block encoded by O_H with some normalization factor $\alpha_H \geq 2\|\mathbf{H}\|_2$. Suppose that oracle $O_\psi |0\rangle = |\psi\rangle$ prepares an initial state within distance $\||\psi\rangle - |\psi_0\rangle\| = \mathcal{O}(\frac{\epsilon}{\alpha_H \alpha_U})$ from an eigenstate $|\psi_0\rangle$ such that $\mathbf{H}|\psi_0\rangle = E_0|\psi_0\rangle$, where

$$\alpha_U \geq \max_{\ell=0,1,\dots,v-1} \|U_\ell(\frac{\mathbf{H}}{\alpha_H})\| \quad (37)$$

is an upper bound on the Chebyshev polynomials of the second kind $U_j(x)$ (E5) with $v = \mathcal{O}(\frac{\alpha_H}{\epsilon})$. Then, E_0 can be estimated with accuracy ϵ and probability $1-p_f$ using

$$\mathcal{O}\left(\frac{\alpha_H}{\epsilon} \alpha_U \log\left(\frac{1}{p_f}\right)\right) \quad (38)$$

queries to controlled- O_H , controlled- O_ψ and their inverses.

Since, similarly to qubitzed-QPE, the procedure requires calling a block encoding of the Hamiltonian, and the query complexity depends on the subnormalization constant of this block encoding, we will outline how to block encode $\tilde{\mathbf{H}}$ using the Pauli LCU decomposition, similar to what was done in the Hermitian case. With the choices made for $g_{\mu_{ne}}$ and $h_{\mu_{ee}}$ in equations (34) and (35), and the expressions derived in Ref. [46], we can proceed as previously and express the transcorrelated Hamiltonian in the basis of the grid points using the Voronoi finite volume scheme:

$$\tilde{\mathbf{H}} = \sum_{i=0}^{\eta-1} \left(\sum_{m,n=0}^{N-1} \left(-\frac{1}{2} \mathbf{L}_{mn} - \tilde{\mathbf{D}}_{mn}^{(ne)} \right) |m\rangle_i \langle n|_i - \sum_{m=0}^{N-1} \tilde{\mathbf{U}}_m |m\rangle_i \langle m|_i - \sum_{j>i}^{\eta-1} \sum_{m,p=0}^{N-1} \tilde{\mathbf{W}}_{mp} |m\rangle_i \langle m|_i |p\rangle_j \langle p|_j \right. \\ \left. - \sum_{j>i}^{\eta-1} \sum_{m,n,p,q=0}^{N-1} \tilde{\mathbf{D}}_{mnpq}^{(ee)} |m\rangle_i \langle n|_i |p\rangle_j \langle q|_j - \sum_{j>i}^{\eta-1} \sum_{k>j>i}^{N-1} \sum_{m,p,t=0}^{N-1} \tilde{\mathbf{B}}_{mpt} |m\rangle_i \langle m|_i |p\rangle_j \langle p|_j |t\rangle_k \langle t|_k \right) \quad (39)$$

where

$$\tilde{\mathbf{D}}_{mn}^{(ne)} = \begin{cases} \sum_{\alpha=0}^{M-1} \frac{-\mathcal{Z}_\alpha + \text{erf}(\mu r_{m\alpha})}{2v_m} \sigma_{mn} \hat{\mathbf{r}}_{mn} \cdot \hat{\mathbf{r}}_{m\alpha} & \text{if } n \in \Lambda(m) \\ 0 & \text{otherwise} \end{cases} \quad (40)$$

$$\tilde{\mathbf{D}}_{mnpq}^{(ee)} = \begin{cases} \frac{1 - \text{erf}(\mu r_{mp})}{2} \left(\frac{\sigma_{mn}}{v_m} \hat{\mathbf{r}}_{mn} - \frac{\sigma_{pq}}{v_p} \hat{\mathbf{r}}_{pq} \right) \cdot \hat{\mathbf{r}}_{mp} & \text{if } n \in \Lambda(m) \text{ and } q \in \Lambda(p) \\ 0 & \text{otherwise} \end{cases} \quad (41)$$

$$\tilde{\mathbf{U}}_m = \sum_{\alpha=0}^{M-1} \left(\frac{-\mathcal{Z}_\alpha + \text{erf}(\mu r_{m\alpha})}{r_{m\alpha}} - \frac{\mu}{\sqrt{\pi}} e^{-(\mu r_{m\alpha})^2} + \frac{(\mathcal{Z}_\alpha - \text{erf}(\mu r_{m\alpha}))^2}{2} \right) \\ + \sum_{\alpha=0}^{M-1} \sum_{\beta=0}^{M-1} \left((\mathcal{Z}_\alpha - \text{erf}(\mu r_{m\alpha})).(\mathcal{Z}_\beta - \text{erf}(\mu r_{m\beta})) \hat{\mathbf{r}}_{m\alpha} \cdot \hat{\mathbf{r}}_{m\beta} \right) \quad (42)$$

$$\tilde{\mathbf{W}}_{mp} = \frac{1 - \text{erf}(\mu r_{mp})}{r_{mp}} + \frac{\mu}{\sqrt{\pi}} e^{-(\mu r_{mp})^2} + \frac{(1 - \text{erf}(\mu r_{mp}))^2}{2} \quad (43)$$

$$\tilde{\mathbf{B}}_{mpt} = (1 - \text{erf}(\mu r_{mp})).(1 - \text{erf}(\mu r_{mt})) \hat{\mathbf{r}}_{mp} \cdot \hat{\mathbf{r}}_{mt} \quad (44)$$

which can be rewritten as

$$\tilde{\mathbf{H}} = \sum_{m,n=0}^{N-1} \tilde{\mathbf{T}}_{mn} \sum_{i=0}^{\eta-1} |m\rangle_i \langle n|_i \\ + \frac{1}{2} \sum_{m,n,p,q=0}^{N-1} \tilde{\mathbf{W}}_{mnpq} \sum_{i \neq j}^{\eta-1} |m\rangle_i \langle n|_i |p\rangle_j \langle q|_j \\ - \frac{1}{3} \sum_{m,p,t=0}^{N-1} \tilde{\mathbf{B}}_{mpt} \sum_{i \neq j \neq k}^{\eta-1} |m\rangle_i \langle m|_i |p\rangle_j \langle p|_j |t\rangle_k \langle t|_k \quad (45)$$

where $\tilde{\mathbf{B}}_{mpt}$ is defined in (44) and

$$\tilde{\mathbf{T}}_{mn} = -\frac{1}{2} \mathbf{L}_{mn} - \tilde{\mathbf{D}}_{mn}^{(ne)} - \begin{cases} \tilde{\mathbf{U}}_m & \text{if } m = n \\ 0 & \text{otherwise.} \end{cases} \quad (46)$$

$$\tilde{\mathbf{W}}_{mnpq} = -\tilde{\mathbf{D}}_{mnpq}^{(ee)} - \begin{cases} \tilde{\mathbf{W}}_{mp} & \text{if } m = n \text{ and } p = q \\ 0 & \text{otherwise} \end{cases} \quad (47)$$

we adopt a similar approach to block encode the transcorrelated Hamiltonian using an adapted LCU

$$\text{decomposition:} \quad \tilde{\mathbf{H}} = \sum_{m,n=0}^{N-1} \tilde{\omega}_{mn} \sum_{i=0}^{\eta-1} \prod_{b=0}^{\log N-1} \mathbf{X}_{i \log N+b}^{m_b} \mathbf{Z}_{i \log N+b}^{n_b} \\ + \frac{1}{2} \sum_{m,n,p,q=0}^{N-1} \tilde{\gamma}_{mnpq} \sum_{i \neq j}^{\eta-1} \prod_{b=0}^{\log N-1} \mathbf{X}_{i \log N+b}^{m_b} \mathbf{Z}_{i \log N+b}^{n_b} \mathbf{X}_{j \log N+b}^{p_b} \mathbf{Z}_{j \log N+b}^{q_b} \\ - \frac{1}{3} \sum_{m,p,t=0}^{N-1} \tilde{\zeta}_{mpt} \sum_{i \neq j \neq k}^{\log N-1} \prod_{b=0}^{\log N-1} \mathbf{Z}_{i \log N+b}^{m_b} \mathbf{Z}_{j \log N+b}^{p_b} \mathbf{Z}_{k \log N+b}^{t_b} \quad (48)$$

The explicit expressions for the coefficients are given by:

$$\tilde{\omega}_{mn} = \frac{1}{N} \sum_{x=0}^{N-1} (-1)^{x \odot n} \tilde{\mathbf{T}}_{m \oplus x, x} \quad (49)$$

$$\tilde{\gamma}_{mnpq} = \frac{1}{N^2} \sum_{x,y=0}^{N-1} (-1)^{(x \odot n) + (y \odot q)} \tilde{\mathbf{W}}_{m \oplus x, x, p \oplus y, y} \quad (50)$$

$$\tilde{\zeta}_{mpt} = \frac{1}{N^3} \sum_{x,y,z=0}^{N-1} (-1)^{(x \odot m) + (y \odot p) + (z \odot t)} \tilde{\mathbf{B}}_{mpt} \quad (51)$$

$$\begin{aligned} \tilde{\mathbf{H}}_{LCU} = & \sum_{m,n=0}^{N-1} \tilde{\omega}'_{mn} \sum_{i=0}^{\eta-1} \prod_{b=0}^{\log N-1} \mathbf{X}_{i \log N+b}^{m_b} \mathbf{Z}_{i \log N+b}^{n_b} + \frac{1}{2} \sum_{m,n,p,q=0}^{N-1} \tilde{\gamma}'_{mnpq} \sum_{i \neq j}^{\eta-1} \prod_{b=0}^{\log N-1} \mathbf{X}_{i \log N+b}^{m_b} \mathbf{Z}_{i \log N+b}^{n_b} \mathbf{X}_{j \log N+b}^{p_b} \mathbf{Z}_{j \log N+b}^{q_b} \\ & - \frac{1}{3} \sum_{m,p,t=1}^{N-1} \tilde{\zeta}'_{mpt} \sum_{i \neq j \neq k}^{\eta-1} \prod_{b=0}^{\log N-1} \mathbf{Z}_{i \log N+b}^{m_b} \mathbf{Z}_{j \log N+b}^{p_b} \mathbf{Z}_{k \log N+b}^{t_b} \end{aligned} \quad (52)$$

where

$$\tilde{\omega}'_{mn} = \begin{cases} 0 & \text{if } m = n = 0 \\ \tilde{\omega}_{0n} + \frac{1}{2}(N-1)(\tilde{\gamma}_{0n00} + \tilde{\gamma}_{000n}) - \frac{1}{3}(N-1)^2(\tilde{\zeta}_{n00} + 2\tilde{\zeta}_{00n}) & \text{if } m = 0 \\ \tilde{\omega}_{mn} + \frac{1}{2}(N-1)(\tilde{\gamma}_{mn00} + \tilde{\gamma}_{00mn}) & \text{otherwise} \end{cases} \quad (53)$$

$$\tilde{\gamma}'_{mnpq} = \begin{cases} 0 & \text{if } m = n = 0 \text{ or } p = q = 0 \\ \tilde{\gamma}_{0n0q} - \frac{1}{3}(N-1)(\tilde{\zeta}_{0nq} + 2\tilde{\zeta}_{nq0}) & \text{if } m = p = 0 \\ \tilde{\gamma}_{mnpq} & \text{otherwise} \end{cases} \quad (54)$$

$$\tilde{\zeta}'_{mpt} = \begin{cases} 0 & \text{if } m = 0 \text{ or } p = 0 \text{ or } t = 0 \\ \tilde{\zeta}_{mpt} & \text{otherwise} \end{cases} \quad (55)$$

Similarly to the two-body LCU expansion derived in [20], one can straightforwardly write one for the three-body term. Note that $\tilde{\mathbf{T}}_{mn}$ and $\tilde{\mathbf{W}}_{mnpq}$ contain non-Hermitian terms, and the latter two-body matrix is no longer diagonal. As before, we remove identity Pauli strings and repeating terms to get fewer coefficients to load. For the three-body term, we have the symmetry $\tilde{\zeta}_{mpt} = \tilde{\zeta}_{mtp}$, which enables to write equations (52) to (55).

V. COMPUTATIONAL DETAILS

This section outlines the numerical setup for the simulations presented in the next section. Voronoi diagrams were generated using the Qhull library [42]. For one-electron Hamiltonians, whose matrices comprise only a few thousand entries, we obtained exact spectra via direct diagonalization with standard linear-algebra routines. Two-electron systems square the Hilbert-space dimension, so we employed the parallel, non-Hermitian Davidson solver [50] in Quantum Package 2.0 [51] to compute ground-state energies and wavefunctions. The initial guess in the Davidson solver was a cc-PVDZ Hartree–Fock solution evaluated on the grid, conformingly with the state-preparation strategy proposed for the quantum algorithm (see Appendix B).

VI. SIMULATIONS

In this section, we present the results of numerical simulations to support our Voronoi finite volume scheme and its transcorrelated extension. We first discuss the impact of the correlation factor on the discretized wave

functions expressed on our real-space grids, and then report some results on energy differences.

Let us begin by investigating the impact of the nucleus-electron correlation factor on the wave function in the case of one-electron systems. We report in Figure 3 the plots of the ground-state wave functions obtained for the H atom and H_2^+ system at 1 Å, with a uniform angular and Becke radial discretization ($\nu = 1$) for 3000 total points, and for various choices of the μ_{ne} parameter tuning the one-body part of τ . As can be seen from Figure 3, the function $g_{\mu_{ne}}$ smooths out the sharp nuclear cusps, and decreasing the parameter μ_{ne} progressively broadens the central peaks, reducing the need for excessively dense grids at the cusps.

Turning now to a two-electron system, we represent in Figure 4 a cutting of the ground-state wavefunction of the helium atom obtained with the method presented in former section, sampled along a circle of radius $\sim 0.5 a_0$ centered on the nucleus, with the second electron fixed at φ close to zero. For the sake of clarity, the amplitudes were obtained with a Gauss–Legendre angular grid, whose separable θ, φ structure makes it straightforward to scan a 1-D cut along φ , albeit less optimal than Lebedev angular grid (as highlighted in the appendix in Fig. 7). In the non-transcorrelated case, the curve shows the familiar sharp cusp anticipated by the electron-electron coalescence condition. As the Jastrow parameter μ_{ee} decreases, the TC transformation progressively smooths this cusp, exactly as predicted by theory and reproducing the results of [46]. Choosing a Jastrow parameter that is too small can introduce anti-correlation effects (as evidenced in [46]), manifested as a maximal electron density at coalescence. Although the transcorrelated Hamiltonian remains isospectral, it is usually preferred to use parameters that preserve a physically meaningful wavefunction.

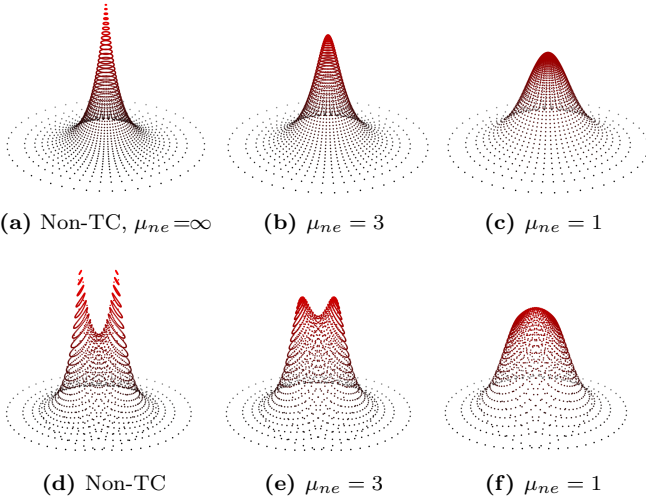


FIG. 3: Sketches of ground-state wavefunctions on a 2-D grid for single-center (top) and two-center (bottom) systems. Columns show the non-transcorrelated case (left) and transcorrelated cases for different values of μ_{ne} .

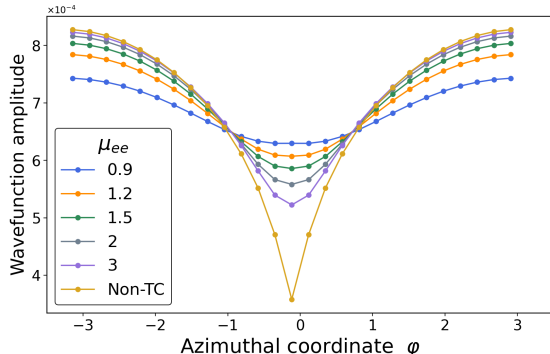


FIG. 4: Cut of the ground-state helium wavefunction sampled along a circle of radius $\sim 0.5 a_0$ centered on the nucleus, with the second electron fixed at the central azimuthal coordinate. The amplitude, plotted versus φ on a Gauss–Legendre angular grid (Voronoi finite-volume discretization), shows a progressively smoother electron–electron cusp as the transcorrelation parameter μ_{ee} increases.

In Figure 5, we report the H_2 potential energy curve of the H_2 molecule as a function of the interatomic distance R , *i.e.* $E(H_2, R) - 2E(H)$. and the results are obtained using the multi-center adaptive grids introduced in Ref. [25]. A grid of roughly 2 000 points, while capturing the qualitative shape, remains far from the exact binding energy; increasing the grid density systematically incorporates more electronic correlation and brings the curve closer to the FCI–CBS reference. An important aspect of the present simulations is that the energies are size-consistent, as evidenced by the dissociation limit correctly approaching zero as the distance R increases. While increasing the radial resolution systematically gives better results at a given

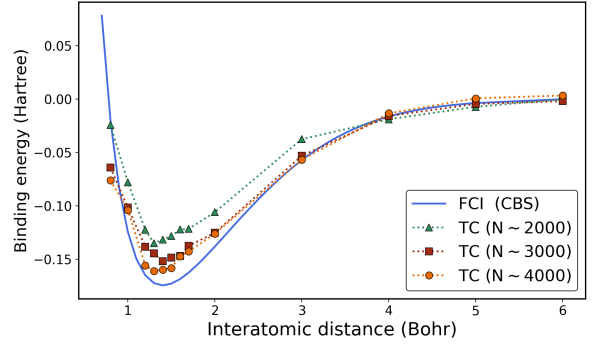


FIG. 5: Dissociation curve of H_2 : binding energy versus internuclear distance for our transcorrelated (TC) method on nonuniform grids, compared to FCI at the CBS limit. Grids studied contain 2000, 3000, and 4000 total points (20, 30, and 40 radial points combined with 50 angular quadrature points per atom), corresponding to Hamiltonian matrices of dimensions 4, 9, and 16 millions, respectively.

geometry, the dissociation curves lack some perfectly smooth behavior across the stretching of the bond. We believe the observed kinks occur because a slight change in bond length can completely reshuffle the Voronoi cells associated to our non-overlapping multicenter grid. This abrupt reorganization sometimes creates locally favorable resolution and sometimes less favorable, directly affecting the computed energy. Further basis-convergence simulations are presented in Appendix C.

VII. DISCUSSION AND OUTLOOK

Real-space methods that explicitly track η electrons on an N -point grid remain rare in standard computational chemistry because they naively require an N^η -dimensional Hilbert space. Using quantum devices, however, this Hilbert space can be encoded using $\eta \log N$ qubits, making fine spatial discretizations (large N) regimes attractive. For example, our H_2 simulation involved diagonalizing matrices as large as 16 million \times 16 million, while the equivalent quantum encoding would use only 12 qubits per electron (4 096 grid points), and every additional pair of qubits doubles the spatial resolution. Since high-accuracy DFT grids rarely exceed 10^5 points per atom, a ten-atom calculation would only require on the order of 20 qubits per electron. This provides an intuitive picture of how compactly the wavefunction can be stored while approaching the continuum limit. Prior such approaches within the Quantum Phase Estimation algorithm have used uniform grids or plane waves to keep Hamiltonian complexity low, but these schemes will likely fail to resolve the cusps in electronic wavefunctions that arise from Coulomb singularities, which are often approximated as bounded trading physical relevance for convenience. In this paper, we integrate nonuniform, molecular adaptive grids into a first-quantized, real-space quantum computing framework for electronic structure calculations. Further

in this direction, we introduce the use of a transcorrelated Hamiltonian, that eliminates Coulombic infinities and corresponding cusps in the eigenvectors. Numerical validation on He and H₂ offers a realistic benchmark on atomic and molecular systems, featuring electron–nuclear and electron–electron cusps, as well as both dynamic and static correlation regimes, and the successful H₂ dissociation suggests that the present real-space, transcorrelated framework could handle other more complex chemical systems. Although detailed scaling analyses and quantitative comparisons to other methods are left for future work, this study establishes a flexible, first-step approach that can be refined and extended in multiple directions.

In the present work, we used a rather minimal set-up both in terms of the definition of the Voronoi cells and the correlation factor, which leaves a substantial room for improvement that we now outline. The Voronoi finite-volume discretization allows to express differential operators in the basis on *any* input grid, producing a Hamiltonian that is sparse yet has generally unstructured off-diagonal elements. Any such operators can be block encoded via Pauli-LCU expansion, but the brute force classical preprocessing to find the coefficients scales with the nonzero elements in the Hamiltonian, thus polynomially in the basis size. Since the introduced molecular grids are typically organized as multicenter shells, they exhibit some regularity. At the same time, efficiently loading structured data onto quantum hardware, whether for state preparation or unitary synthesis, remains an active research area, with a growing diversity of data structures now amenable to efficient encoding [52–54]. Exploiting these grid symmetries alongside tailored data-loading schemes will be crucial for scaling this approach. Alternatively, a fully quantum workflow, with no classical preprocessing, could take as input the grid parameters (nuclear coordinates, radial and angular point counts, and related settings) and, via quantum arithmetics [55], construct the Voronoi diagram, assemble the Hamiltonian matrix elements, and then compute the Pauli-LCU coefficients from Eq. D using basic quantum gates (e.g., SWAP, Hadamard) as outlined in [43]. Such an approach will demand a careful resource analysis. Classical computational

chemistry has long optimized DFT integration grids and transcorrelated Hamiltonian forms, with Jastrow parameter selection being its own discipline. Likewise, optimizing grids and Jastrow choices on our numerical scheme should improve these baseline simulations.

Transcorrelated Hamiltonians have previously been proposed on quantum computers through imaginary time evolution using Gaussian basis sets [56–58]. Since transcorrelated Hamiltonians are inherently derived in real space, we believe that our real-space encoding offers a more natural representation. Coupled with the Quantum Eigenvalue Estimation (QEVE) algorithm that offers deterministic eigenvalue extraction, we anticipate this scheme to become a promising pathway to optimally exploit the transcorrelated method on quantum computers. Together with the efficient real-space sampling with molecule-adaptive grids, this framework establishes a robust and flexible foundation for achieving complete-basis-set-limit accuracy in ground-state quantum chemistry on future quantum hardware.

ACKNOWLEDGMENTS

This work has received funding from the European Research Council (ERC) under the European Union’s Horizon 2020 research and innovation program (grant agreement No 810367), project EMC2 (JPP). Support from the PEPR EPIQ - Quantum Software (ANR-22-PETQ-0007, JPP) and HQI (JPP) programs is acknowledged. The authors wish to thank Yvon Maday, Igor Chollet, Pierre Monmarché and Solal Perrin-Roussel for fruitful discussions.

COMPETING INTERESTS

JPP is shareholder and co-founder of Qubit Pharmaceuticals. The remaining authors declare no other competing interests.

-
- [1] Richard P. Feynman. Simulating physics with computers. *Int. J. Theor. Phys.*, 21(6/7), 2018. pp. 133–153.
 - [2] A Yu Kitaev. Quantum measurements and the abelian stabilizer problem. *arXiv preprint quant-ph/9511026*, 1995.
 - [3] James D Whitfield, Jacob Biamonte, and Alán Aspuru-Guzik. Simulation of electronic structure hamiltonians using quantum computers. *Molecular Physics*, 109(5):735–750, 2011.
 - [4] Alán Aspuru-Guzik, Alán D. Dutoi, Peter J. Love, and Martin Head-Gordon. Simulated quantum computation of molecular energies. *Science*, 309(5741):1704–1707, 2005.
 - [5] David Wecker, Brian K. Clark, Matthew B. Hastings, and Matthias Troyer. Gate-count estimates for performing quantum chemistry on small quantum computers. *Physical Review A*, 90(2):022305, 2014.
 - [6] Ryan Babbush, Jarrod McClean, Dave Wecker, Alán Aspuru-Guzik, and Nathan Wiebe. Chemical basis of Trotter-Suzuki errors in quantum chemistry simulation. *Physical Review A*, 91(2):022311, 2015.
 - [7] Guang Hao Low, Yuan Su, Yu Tong, and Minh C Tran. Complexity of implementing trotter steps. *PRX Quantum*, 4(2):020323, 2023.
 - [8] Dominic W Berry, Andrew M Childs, Richard Cleve, Robin Kothari, and Rolando D Somma. Simulating hamiltonian dynamics with a truncated Taylor series. *Physical Review Letters*, 114(9):090502, 2015.
 - [9] Ryan Babbush, Nathan Wiebe, Jarrod McClean, James McClain, Hartmut Neven, and Garnet Kin-Lic Chan. Low-depth quantum simulation of materials. *Physical Review X*, 8(1):011044, 2018.

- [10] Guang Hao Low and Isaac L Chuang. Hamiltonian simulation by qubitization. *Quantum*, 3:163, 2019.
- [11] Ryan Babbush, William J Huggins, Dominic W Berry, Shu Fay Ung, Andrew Zhao, David R Reichman, Hartmut Neven, Andrew D Baczewski, and Joonho Lee. Quantum simulation of exact electron dynamics can be more efficient than classical mean-field methods. *Nature Communications*, 14(1):4058, 2023.
- [12] Diata Traore, Olivier Adjoua, César Feniou, Ioanna-Maria Lygatsika, Yvon Maday, Evgeny Posenitskiy, Kerstin Hammernik, Alberto Peruzzo, Julien Toulouse, Emmanuel Giner, and Jean-Philip Piquemal. Shortcut to chemically accurate quantum computing via density-based basis-set correction. *Communications Chemistry*, 7(1):269, 2024.
- [13] Yuan Su, Dominic W Berry, Nathan Wiebe, Nicholas Rubin, and Ryan Babbush. Fault-tolerant quantum simulations of chemistry in first quantization. *PRX Quantum*, 2(4):040332, 2021.
- [14] Ivan Kassal, Stephen P Jordan, Peter J Love, Masoud Mohseni, and Alán Aspuru-Guzik. Polynomial-time quantum algorithm for the simulation of chemical dynamics. *Proceedings of the National Academy of Sciences*, 105(48):18681–18686, 2008.
- [15] Ian D Kivlichan, Nathan Wiebe, Ryan Babbush, and Alán Aspuru-Guzik. Bounding the costs of quantum simulation of many-body physics in real space. *Journal of Physics A: Mathematical and Theoretical*, 50(30):305301, 2017.
- [16] Hans Hon Sang Chan, Richard Meister, Tyson Jones, David P Tew, and Simon C Benjamin. Grid-based methods for chemistry simulations on a quantum computer. *Science Advances*, 9(9):eab07484, 2023.
- [17] Andrew M Childs, Jiaqi Leng, Tongyang Li, Jin-Peng Liu, and Chenyi Zhang. Quantum simulation of real-space dynamics. *Quantum*, 6:860, 2022.
- [18] Ryan Babbush, Dominic W Berry, Jarrod R McClean, and Hartmut Neven. Quantum simulation of chemistry with sublinear scaling in basis size. *npj Quantum Information*, 5(1):92, 2019.
- [19] Dominic W Berry, Nicholas C Rubin, Ahmed O Elnabawy, Gabriele Ahlers, A Eugene DePrince III, Joonho Lee, Christian Gogolin, and Ryan Babbush. Quantum simulation of realistic materials in first quantization using non-local pseudopotentials. *npj Quantum Information*, 10(1):130, 2024.
- [20] Timothy N Georges, Marius Bothe, Christoph Sünderhauf, Bjorn K Berntson, Róbert Izsák, and Aleksei V Ivanov. Quantum simulations of chemistry in first quantization with any basis set. *npj Quantum Information*, 11(1):55, 2025.
- [21] Norman Troullier and José Luís Martins. Efficient pseudopotentials for plane-wave calculations. *Physical Review B*, 43(3):1993, 1991.
- [22] Jarrod R McClean, Fabian M Faulstich, Qinyi Zhu, Bryan O’Gorman, Yiheng Qiu, Steven R White, Ryan Babbush, and Lin Lin. Discontinuous Galerkin discretization for quantum simulation of chemistry. *New Journal of Physics*, 22(9):093015, 2020.
- [23] Axel D Becke. A multicenter numerical integration scheme for polyatomic molecules. *The Journal of Chemical Physics*, 88(4):2547–2553, 1988.
- [24] Michael E Mura and Peter J Knowles. Improved radial grids for quadrature in molecular density-functional calculations. *Journal of Chemical Physics*, 104(24):9848–9858, 1996.
- [25] N Sukumar. Voronoï cell finite difference method for the diffusion operator on arbitrary unstructured grids. *International Journal for Numerical Methods in Engineering*, 57(1):1–34, 2003.
- [26] Sang-Kil Son. Voronoï-cell finite difference method for accurate electronic structure calculation of polyatomic molecules on unstructured grids. *Journal of Computational Physics*, 230(5):2160–2173, 2011.
- [27] Sang-Kil Son and Shih-I Chu. Theoretical study of orientation-dependent multiphoton ionization of polyatomic molecules in intense ultrashort laser fields: A new time-dependent Voronoï-cell finite difference method. *Chemical Physics*, 366(1-3):91–102, 2009.
- [28] Samuel Francis Boys and Nicholas Charles Handy. The determination of energies and wavefunctions with full electronic correlation. *Proceedings of the Royal Society of London. A. Mathematical and Physical Sciences*, 310(1500):43–61, 1969.
- [29] Guang Hao Low and Yuan Su. Quantum eigenvalue processing. In *2024 IEEE 65th Annual Symposium on Foundations of Computer Science (FOCS)*, page 1051–1062. IEEE, October 2024.
- [30] M. Born and R. Oppenheimer. Zur quantentheorie der moleküle. *Annalen der Physik*, 389(20):457–484, 1927.
- [31] Trygve Helgaker, Poul Jørgensen, and Jeppe Olsen. *Molecular Electronic-Structure Theory*. John Wiley & Sons, Chichester, UK, 2000.
- [32] Dominic W. Berry, Mária Kieferová, Artur Scherer, Yuval R. Sanders, Guang Hao Low, Nathan Wiebe, Craig Gidney, and Ryan Babbush. Improved techniques for preparing eigenstates of fermionic hamiltonians. *npj Quantum Information*, 4(1), May 2018.
- [33] Charlotte Froese Fischer. *The Hartree-Fock method for atoms: A numerical approach*. John Wiley and Sons, Inc., 1976.
- [34] Osamu Matsuoka. Grid points of Gauss-Legendre quadrature as exponent parameters of basis functions of atomic Hartree-Fock wavefunctions. *Chemical Physics Letters*, 77(2):387–389, 1981.
- [35] CHL Beentjes. Quadrature on a spherical surface (2015). Working note available on the website <http://people.maths.ox.ac.uk/beentjes/Essays>.
- [36] Qiang Du, Max D. Gunzburger, and Lili Ju. Voronoï-based finite volume methods, optimal Voronoï meshes, and pdes on the sphere. *Computer Methods in Applied Mechanics and Engineering*, 192(35):3933–3957, 2003.
- [37] Leonardo A Poveda and Pedro Peixoto. On pointwise error estimates for Voronoï-based finite volume methods for the poisson equation on the sphere. *Advances in Computational Mathematics*, 49(3):36, 2023.
- [38] Franz Aurenhammer. Voronoï diagrams—a survey of a fundamental geometric data structure. *ACM Comput. Surv.*, 23(3):345–405, September 1991.
- [39] Qiang Du, Maria Emelianenko, and Lili Ju. Convergence of the Lloyd algorithm for computing centroidal Voronoï tessellations. *SIAM Journal on Numerical Analysis*, 44(1):102–119, 2006.
- [40] Qiang Du, Vance Faber, and Max Gunzburger. Centroidal Voronoï tessellations: Applications and algorithms. *SIAM Review*, 41(4):637–676, 1999.
- [41] David Arthur and Sergei Vassilvitskii. How slow is the k-means method? In *Proceedings of the Twenty-Second Annual Symposium on Computational Geometry, SCG ’06*, page 144–153, New York, NY, USA, 2006. Association for Computing Machinery.
- [42] Qhull. <http://www.qhull.org/>.
- [43] Timothy N Georges, Bjorn K Berntson, Christoph Sünderhauf, and Aleksei V Ivanov. Pauli decomposition via the fast Walsh-Hadamard transform. *New Journal of Physics*, 27(3):033004, February 2025.
- [44] Marcel Nooijen and Rodney J Bartlett. Elimination of coulombic infinities through transformation of the

- hamiltonian. *The Journal of Chemical Physics*, 109(19):8232–8240, 1998.
- [45] Aron J. Cohen, Hongjun Luo, Kai Guther, Werner Dobrautz, David P. Tew, and Ali Alavi. Similarity transformation of the electronic Schrödinger equation via jastrow factorization. *The Journal of Chemical Physics*, 151(6):061101, 08 2019.
- [46] Emmanuel Giner. A new form of transcorrelated hamiltonian inspired by range-separated DFT. *The Journal of Chemical Physics*, 154(8), February 2021.
- [47] Tosio Kato. On the eigenfunctions of many-particle systems in quantum mechanics. *Communications on Pure and Applied Mathematics*, 10(2):151–177, 1957.
- [48] Changpeng Shao. Computing eigenvalues of diagonalizable matrices on a quantum computer. *ACM Transactions on Quantum Computing*, 3(4):1–20, 2022.
- [49] Changpeng Shao and Jin-Peng Liu. Solving generalized eigenvalue problems by ordinary differential equations on a quantum computer. *Proceedings of the Royal Society A*, 478(2262):20210797, 2022.
- [50] M. Crouzeix, B. Philippe, and M. Sadkane. The Davidson method. *SIAM Journal on Scientific Computing*, 15(1):62–76, 1994.
- [51] Yann Garniron, Thomas Applencourt, Kevin Gasperich, Anouar Benali, Anthony Ferté, Julien Paquier, Barthélémy Pradines, Roland Assaraf, Peter Reinhardt, Julien Toulouse, Pierrette Barbaresco, Nicolas Renon, Grégoire David, Jean-Paul Malrieu, Mickaël Vérité, Michel Caffarel, Pierre-François Loos, Emmanuel Giner, and Anthony Scemama. Quantum Package 2.0: An open-source determinant-driven suite of programs. *Journal of Chemical Theory and Computation*, 15(6):3591–3609, 2019. PMID: 31082265.
- [52] Christoph Sünderhauf, Earl Campbell, and Joan Camps. Block-encoding structured matrices for data input in quantum computing. *Quantum*, 8:1226, 2024.
- [53] Julien Zylberman, Ugo Nzongani, Andrea Simonetto, and Fabrice Debbasch. Efficient quantum circuits for non-unitary and unitary diagonal operators with space-time-accuracy trade-offs. *ACM Transactions on Quantum Computing*, 6(2):1–43, 2025.
- [54] Dominic W. Berry, Craig Gidney, Mario Motta, Jarrod R. McClean, and Ryan Babbush. Qubitization of arbitrary basis quantum chemistry leveraging sparsity and low rank factorization. *Quantum*, 3:208, December 2019.
- [55] M. A. Nielsen and I. L. Chuang. *Quantum Computation and Quantum Information*. Cambridge University Press, 2000.
- [56] Sam McArdle and David P Tew. Improving the accuracy of quantum computational chemistry using the transcorrelated method. *arXiv preprint arXiv:2006.11181*, 2020.
- [57] Werner Dobrautz, Igor O Sokolov, Ke Liao, Pablo López Ríos, Martin Rahm, Ali Alavi, and Ivano Tavernelli. Toward real chemical accuracy on current quantum hardware through the transcorrelated method. *Journal of Chemical Theory and Computation*, 20(10):4146–4160, 2024.
- [58] Igor O. Sokolov, Werner Dobrautz, Hongjun Luo, Ali Alavi, and Ivano Tavernelli. Orders of magnitude increased accuracy for quantum many-body problems on quantum computers via an exact transcorrelated method. *Phys. Rev. Res.*, 5:023174, Jun 2023.
- [59] César Feniou, Olivier Adjoua, Baptiste Claudon, Julien Zylberman, Emmanuel Giner, and Jean-Philip Piquemal. Sparse quantum state preparation for strongly correlated systems. *The Journal of Physical Chemistry Letters*, 15(11):3197–3205, 2024.
- [60] Norm M. Tubman, Carlos Mejuto-Zaera, Jeffrey M. Epstein, Diptarka Hait, Daniel S. Levine, William Huggins, Zhang Jiang, Jarrod R. McClean, Ryan Babbush, Martin Head-Gordon, and K. Birgitta Whaley. Postponing the orthogonality catastrophe: efficient state preparation for electronic structure simulations on quantum devices. *arXiv preprint arXiv:1809.05523*, 2018.
- [61] Stepan Fomichev, Kasra Hejazi, Modjtaba Shokrian Zini, Matthew Kiser, Joana Fraxanet Morales, Pablo Antonio Moreno Casares, Alain Delgado, Joonsuk Huh, Arne-Christian Voigt, Jonathan E. Mueller, and Juan Miguel Arrazola. Initial state preparation for quantum chemistry on quantum computers. *arXiv preprint arXiv:2310.18410*, 2023.
- [62] Danial Motlagh and Nathan Wiebe. Generalized quantum signal processing. *PRX Quantum*, 5:020368, Jun 2024.
- [63] Julien Zylberman and Fabrice Debbasch. Efficient quantum state preparation with Walsh series. *Physical Review A*, 109(4):042401, 2024.
- [64] Adam Holmes and A. Y. Matsuura. Efficient Quantum Circuits for Accurate State Preparation of Smooth, Differentiable Functions . In *2020 IEEE International Conference on Quantum Computing and Engineering (QCE)*, pages 169–179, Los Alamitos, CA, USA, October 2020. IEEE Computer Society.
- [65] Bao Yan, Shijie Wei, Haocong Jiang, Hong Wang, Qianheng Duan, Zhi Ma, and Gui-Lu Long. Fixed-point oblivious quantum amplitude-amplification algorithm. *Scientific Reports*, 12(1):14339, Aug 2022.
- [66] Christoph Sünderhauf. Generalized quantum singular value transformation. *arXiv preprint arXiv:2312.00723*, 2023.
- [67] George Arfken. *Mathematical Methods for Physicists*. Academic Press, Inc., San Diego, third edition, 1985.
- [68] Pedro C.S. Costa, Dong An, Yuval R. Sanders, Yuan Su, Ryan Babbush, and Dominic W. Berry. Optimal scaling quantum linear-systems solver via discrete adiabatic theorem. *PRX Quantum*, 3:040303, Oct 2022.

Appendix A: Expression of Differential Operators in the Voronoi Finite Volume Scheme

Consider the molecular Schrödinger equation in (1) and (2):

$$\sum_{i=0}^{\eta-1} \left(-\frac{1}{2} \nabla_{\mathbf{x}_i}^2 \Psi(\dots, \mathbf{x}_i, \dots) - \sum_{\alpha=0}^{M-1} \frac{\mathcal{Z}_{\alpha}}{|\mathbf{x}_i - \mathbf{R}_{\alpha}|} \Psi(\dots, \mathbf{x}_i, \dots) + \sum_{j>i}^{\eta-1} \frac{1}{|\mathbf{x}_i - \mathbf{x}_j|} \Psi(\dots, \mathbf{x}_i, \dots) \right) = E \Psi(\dots, \mathbf{x}_i, \dots) \quad (\text{A1})$$

and suppose the entire space of interest is filled with arbitrarily distributed points $\{\mathbf{r}_m\}_{m=0}^{N-1}$, forming a Voronoi diagram in \mathbb{R}^3 . We take the volume integral over the Voronoi cells $\{\text{Vor}(\mathbf{r}_{m_i})\}_{i=0}^{\eta-1}$ occupied by each electron on both sides:

$$\begin{aligned} & \sum_{i=0}^{\eta-1} \left(-\frac{1}{2} \int_{\text{Vor}(\mathbf{r}_{m_0})} \dots \int_{\text{Vor}(\mathbf{r}_{m_i})} \dots \int_{\text{Vor}(\mathbf{r}_{m_{\eta-1}})} \nabla_{\mathbf{x}_i}^2 \Psi(\mathbf{x}_0, \dots, \mathbf{x}_i, \dots, \mathbf{x}_{\eta-1}) d\mathbf{x}_0 \dots d\mathbf{x}_i \dots d\mathbf{x}_{\eta-1} \right. \\ & \quad \left. - \sum_{\alpha=0}^{M-1} \int_{\text{Vor}(\mathbf{r}_{m_0})} \dots \int_{\text{Vor}(\mathbf{r}_{m_i})} \dots \int_{\text{Vor}(\mathbf{r}_{m_{\eta-1}})} \frac{\mathcal{Z}_{\alpha}}{|\mathbf{x}_i - \mathbf{R}_{\alpha}|} \Psi(\mathbf{x}_0, \dots, \mathbf{x}_i, \dots, \mathbf{x}_{\eta-1}) d\mathbf{x}_0 \dots d\mathbf{x}_i \dots d\mathbf{x}_{\eta-1} \right. \\ & \quad \left. + \sum_{j>i}^{\eta-1} \int_{\text{Vor}(\mathbf{r}_{m_0})} \dots \int_{\text{Vor}(\mathbf{r}_{m_i})} \dots \int_{\text{Vor}(\mathbf{r}_{m_{\eta-1}})} \frac{1}{|\mathbf{x}_i - \mathbf{x}_j|} \Psi(\mathbf{x}_0, \dots, \mathbf{x}_i, \dots, \mathbf{x}_{\eta-1}) d\mathbf{x}_0 \dots d\mathbf{x}_i \dots d\mathbf{x}_{\eta-1} \right) \\ & = E \int_{\text{Vor}(\mathbf{r}_{m_0})} \dots \int_{\text{Vor}(\mathbf{r}_{m_i})} \dots \int_{\text{Vor}(\mathbf{r}_{m_{\eta-1}})} \Psi(\mathbf{x}_0, \dots, \mathbf{x}_i, \dots, \mathbf{x}_{\eta-1}) d\mathbf{x}_0 \dots d\mathbf{x}_i \dots d\mathbf{x}_{\eta-1} \end{aligned} \quad (\text{A2})$$

According to the divergence theorem applied to a gradient field, we can express the main integral of the first term inside the sum as

$$\int_{\text{Vor}(\mathbf{r}_{m_i})} \nabla_{\mathbf{x}_i}^2 \Psi(\dots, \mathbf{x}_i, \dots) d\mathbf{x}_i = \int_{\partial \text{Vor}(\mathbf{r}_{m_i})} \nabla_{\mathbf{x}_i} \Psi(\dots, \mathbf{x}_i, \dots) \cdot d\mathbf{s}_{m_i} = \sum_{n_i \in \Lambda(m_i)} \int_{\Gamma_{m_i n_i}} \nabla_{\mathbf{x}_i} \Psi(\dots, \mathbf{x}_i, \dots) \cdot \hat{\mathbf{r}}_{m_i n_i} d\sigma_{m_i n_i} \quad (\text{A3})$$

where $d\mathbf{s}_{m_i}$ is the unit normal area vector of the boundary $\partial \text{Vor}(\mathbf{r}_{m_i})$ of the Voronoi cell $\text{Vor}(\mathbf{r}_{m_i})$. In the last equality, we decomposed this boundary as the union of the Voronoi facets $\Gamma_{m_i n_i}$ with all surrounding neighbors to $\text{Vor}(\mathbf{r}_{m_i})$, ie $\partial \text{Vor}(\mathbf{r}_{m_i}) = \bigcup_{n_i \in \Lambda(m_i)} \Gamma_{m_i n_i}$. Note that the unit normal vector $\hat{\mathbf{r}}_{m_i n_i} = (\mathbf{r}_{n_i} - \mathbf{r}_{m_i}) / |\mathbf{r}_{n_i} - \mathbf{r}_{m_i}|$ is a normal vector of the facet $\Gamma_{m_i n_i}$. Now, we divide equation (A2) by the product of the volumes of the Voronoi cells $\{v_{m_i}\}_{i=1}^{\eta}$, and take the limit when each one goes to zero. This consists in evaluating the integrands at the discrete points, multiplied by the integration measure and divided by the product of volumes. For one of the terms in the sum of equation (A3), this gives

$$\lim_{v_{m_i} \rightarrow 0} \frac{1}{v_{m_i}} \int_{\Gamma_{m_i n_i}} \nabla_{\mathbf{x}_i} \Psi(\mathbf{x}_1, \dots, \mathbf{x}_i, \dots, \mathbf{x}_{\eta}) \cdot \hat{\mathbf{r}}_{m_i n_i} d\sigma_{m_i n_i} = \frac{1}{v_{m_i}} \nabla_{\mathbf{r}_{m_i}} \Psi(\mathbf{x}_1, \dots, \mathbf{x}_{i-1}, \mathbf{r}_{m_i}, \mathbf{x}_{i+1}, \dots, \mathbf{x}_{\eta}) \cdot \hat{\mathbf{r}}_{m_i n_i} \sigma_{m_i n_i} \quad (\text{A4})$$

Proceeding similarly with all other terms, one gets

$$\begin{aligned} & \sum_{i=0}^{\eta-1} \left(-\frac{1}{2v_{m_i}} \sum_{n_i \in \Lambda(m_i)} \nabla_{\mathbf{r}_{m_i}} \Psi(\mathbf{r}_{m_0}, \dots, \mathbf{r}_{m_i}, \dots, \mathbf{r}_{m_{\eta-1}}) \cdot \hat{\mathbf{r}}_{m_i n_i} \sigma_{m_i n_i} - \sum_{\alpha=0}^{M-1} \frac{\mathcal{Z}_{\alpha}}{|\mathbf{r}_{m_i} - \mathbf{R}_{\alpha}|} \Psi(\mathbf{r}_{m_0}, \dots, \mathbf{r}_{m_i}, \dots, \mathbf{r}_{m_{\eta-1}}) \right. \\ & \quad \left. + \sum_{j>i}^{\eta-1} \frac{1}{|\mathbf{r}_{m_i} - \mathbf{r}_{m_j}|} \Psi(\mathbf{r}_{m_0}, \dots, \mathbf{r}_{m_i}, \dots, \mathbf{r}_{m_{\eta-1}}) \right) = E \Psi(\mathbf{r}_{m_0}, \dots, \mathbf{r}_{m_i}, \dots, \mathbf{r}_{m_{\eta-1}}) \end{aligned} \quad (\text{A5})$$

The continuous problem in (A1) has thus been reduced to a discretized scheme on the Voronoi diagram. We also approximate the directional derivative with a finite difference, whose error can easily be identified using Taylor's theorem:

$$\nabla_{\mathbf{r}_{m_i}} \Psi(\mathbf{r}_{m_0}, \dots, \mathbf{r}_{m_i}, \dots, \mathbf{r}_{m_{\eta-1}}) \cdot \hat{\mathbf{r}}_{m_i n_i} = \frac{\Psi(\mathbf{r}_{m_0}, \dots, \mathbf{r}_{n_i}, \dots, \mathbf{r}_{m_{\eta-1}}) - \Psi(\mathbf{r}_{m_0}, \dots, \mathbf{r}_{m_i}, \dots, \mathbf{r}_{m_{\eta-1}})}{|\mathbf{r}_{n_i} - \mathbf{r}_{m_i}|} + \mathcal{O}(|\mathbf{r}_{n_i} - \mathbf{r}_{m_i}|) \quad (\text{A6})$$

Combining equations (A5) and (A6), we find the expression of the discretized laplacian operator in (15) and that of the scalar potential energy operators. For the gradient operator, similarly to what done in (A3) and (A4), and using an alternative form of the divergence theorem:

$$\begin{aligned} \lim_{v_{m_i} \rightarrow 0} \frac{1}{v_{m_i}} \int_{\text{Vor}(\mathbf{r}_{m_i})} \nabla_{\mathbf{x}_i} \Psi(\dots, \mathbf{x}_i, \dots) d\mathbf{x}_i &= \lim_{v_{m_i} \rightarrow 0} \frac{1}{v_{m_i}} \int_{\partial \text{Vor}(\mathbf{r}_{m_i})} \Psi(\dots, \mathbf{x}_i, \dots)|_{\partial \text{Vor}(\mathbf{r}_{m_i})} d\mathbf{s}_{m_i} \\ &= \sum_{n_i \in \Lambda(m_i)} \lim_{v_{m_i} \rightarrow 0} \frac{1}{v_{m_i}} \int_{\Gamma_{m_i n_i}} \Psi(\dots, \mathbf{x}_i, \dots)|_{\Gamma_{m_i n_i}} \hat{\mathbf{r}}_{m_i n_i} d\sigma_{m_i n_i} \\ &= \sum_{n_i \in \Lambda(m_i)} \frac{1}{v_{m_i}} \Psi(\mathbf{r}_{m_1}, \dots, \mathbf{r}_{m_i}, \dots, \mathbf{r}_{m_\eta})|_{\Gamma_{m_i n_i}} \hat{\mathbf{r}}_{m_i n_i} \sigma_{m_i n_i} \end{aligned} \quad (\text{A7})$$

We approximate the value of the wavefunction on the facet $\Gamma_{m_i n_i}$ by the average value

$$\Psi(\mathbf{r}_{m_0}, \dots, \mathbf{r}_{m_i}, \dots, \mathbf{r}_{m_{\eta-1}})|_{\Gamma_{m_i n_i}} \approx \frac{\Psi(\mathbf{r}_{m_0}, \dots, \mathbf{r}_{m_i}, \dots, \mathbf{r}_{m_{\eta-1}}) + \Psi(\mathbf{r}_{m_0}, \dots, \mathbf{r}_{n_i}, \dots, \mathbf{r}_{m_{\eta-1}})}{2} \quad (\text{A8})$$

Knowing that $\sum_{n_i} \hat{\mathbf{r}}_{m_i n_i} \sigma_{m_i n_i} = 0$ for any convex polygon, the matrix form of the gradient operator projected on a unit vector $\hat{\mathbf{z}}$, *ie* the matrix representation of the directional derivative along $\hat{\mathbf{z}}$, is given by:

$$\mathbf{D}_{mn}^{(\hat{\mathbf{z}})} = \begin{cases} \frac{\sigma_{mn}}{2v_m} \frac{\mathbf{r}_m - \mathbf{r}_n}{|\mathbf{r}_m - \mathbf{r}_n|} \cdot \hat{\mathbf{z}} & \text{if } n \in \Lambda(m) \\ 0 & \text{otherwise} \end{cases} \quad (\text{A9})$$

Appendix B: Initial state

In second-quantized encoding, qubits directly represent orbital occupations, making the Hartree–Fock (HF) determinant trivial to prepare. When stronger ground-state support is needed, various techniques exist to load correlated CI states within the second-quantized formalism [59–61]. First-quantized, real-space encoding requires classically computed molecular orbitals to be evaluated over the chosen discretisation, and the corresponding amplitudes loaded to the computational basis of the qubit register. Then, a fermionic antisymmetrization circuit of size $\mathcal{O}(\eta \log \eta \log N)$ and depth $\mathcal{O}(\log \eta \log \log N)$ is applied to the single-electron registers. The key task is efficient loading of Gaussian orbital amplitudes onto the computational basis, a task that can be addressed through careful grid points / Voronoi cell ordering and advanced state loading routines [62–64]. Likewise, CI wavefunctions can be prepared by first loading each Slater determinant with the above procedure and then assembling the CI state using the standard LCU approach with `PREPARE` and `SELECT` oracles.

Appendix C: Further Basis Convergence Simulations

Figure 6 compares the convergence of the hydrogen ground-state energy for three Becke–Lebedev radial exponents $\nu = 1, 2, 3$. Panel (a) shows the non-transcorrelated Hamiltonian, while (b) and (c) use TC Hamiltonians with $\mu_{ne} = 3$ and $\mu_{ne} = 1$, respectively. In each plot the error (in Hartree) is plotted on a logarithmic scale versus the total number of grid points N . The blue band indicates chemical accuracy (≤ 1 mHa) to the FCI-CBS. Introducing the Jastrow factor accelerates convergence, and reducing μ_{ne} ($\mu_{ne} = 1$) achieves the chemical-accuracy threshold several thousand points sooner than the non-TC case. Across all settings the grid with $\nu = 1$ consistently outperforms higher exponents.

Figure 7 compares the energy convergence of the transcorrelated helium ground state on Gauss–Legendre and Lebedev radial grids. The Lebedev grid several shells earlier than Gauss–Legendre at the same angular resolution, highlighting its better point distribution. As typical in grid-based approaches, the computed energy approaches the full-CI complete-basis-set limit “from below,” with smaller grids underestimating the true energy and each refinement incrementally raising the value toward the FCI-CBS limit.

Appendix D: Block Encoding Procedure

Definition D.1 (Linear Combination of Unitaries). Given the matrix representation $\mathbf{H} \in \mathbb{C}^{N \times N}$ of the Hamiltonian (or any other operator), which can be decomposed into a linear combination of unitaries (LCU), *ie* for $L \leq N^2$ and

$$\mathbf{H} = \sum_{l=0}^{L-1} a_l \mathbf{U}_l \quad (\text{D1})$$

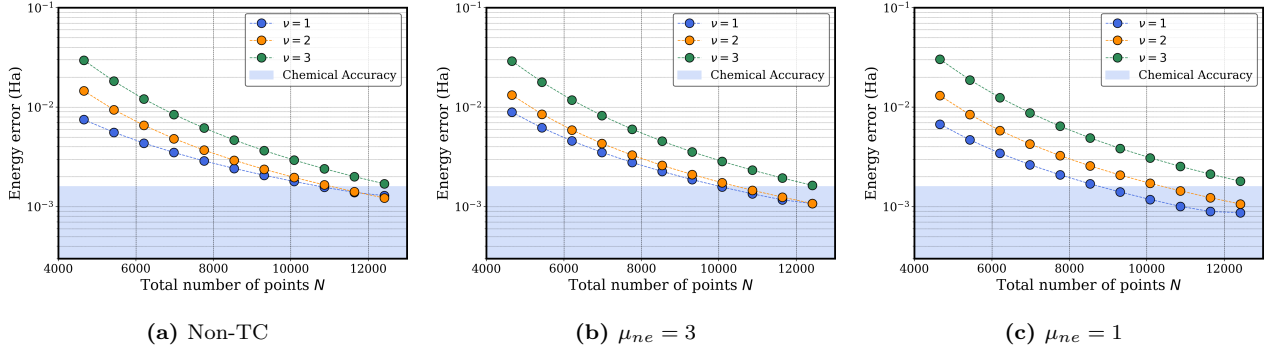


FIG. 6: Convergence of the hydrogen ground-state energy for Becke–Lebedev grids with radial exponents $\nu = 1$ (blue), $\nu = 2$ (orange), and $\nu = 3$ (green). The shaded band marks chemical accuracy (1 mHa). Panels compare the non-transcorrelated (a) and transcorrelated Hamiltonians with $\mu_{ne} = 3$ (b) and $\mu_{ne} = 1$ (c).

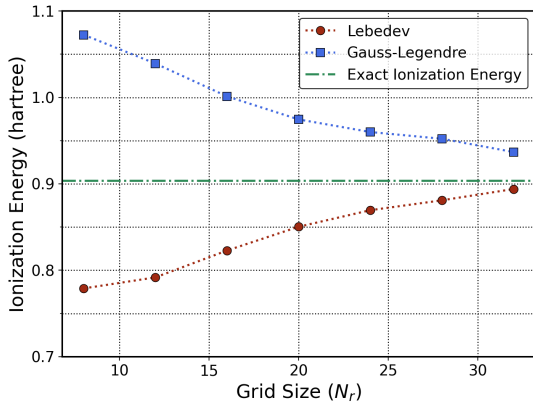


FIG. 7: Convergence of the transcorrelated helium first ionization energy with radial grid size for Gauss–Legendre and Lebedev quadratures (128 angular points each, $\mu_{ee} = 2$, $\mu_{ne} = 1$). The dashed line marks the complete-basis-set full-CI energy of He.

where a_l are some complex coefficients and \mathbf{U}_l are $N \times N$ unitary operators, we define the one-norm of the LCU of \mathbf{H} as

$$\lambda = \sum_{l=0}^{L-1} |a_l| \quad (\text{D2})$$

Definition D.2 (Block Encoding of Square Matrices). We refer to \mathbf{U}_H as a $(\lambda, \kappa, \epsilon)$ -block encoding of $\mathbf{H} \in \mathbb{C}^{N \times N}$ with $\lambda > 0$ and $\epsilon > 0$ if we have

$$\left\| \frac{\mathbf{H}}{\lambda} - (\langle 0 |^{\otimes \kappa} \otimes \mathbf{I}_N) \mathbf{U}_H (\langle 0 |^{\otimes \kappa} \otimes \mathbf{I}_N) \right\|_2 \leq \epsilon \quad (\text{D3})$$

\mathbf{I}_N is the N by N identity matrix. Sandwiching $\mathbf{U}_H \in \mathbb{C}^{2^\kappa N \times 2^\kappa N}$ between $|0\rangle^{\otimes \kappa} \otimes \mathbf{I}_N$ and its bra counterpart is just a mathematical way of saying that we extract the upper left N by N block of \mathbf{U}_H . When the block-encoding is exact, *ie* $\epsilon = 0$, \mathbf{U}_H becomes a (λ, κ) block encoding and it takes the form

$$\mathbf{U}_H = \begin{pmatrix} \mathbf{H}/\lambda & * \\ * & * \end{pmatrix} \quad (\text{D4})$$

where the blocks denoted by '*' do not contain useful information but ensure unitarity. A block encoding \mathbf{U}_H of \mathbf{H} can be obtained by combining the operators PREP (preparation) and SELECT operations defined as [10]:

$$\text{PREP } |0\rangle^{\otimes \log L} = \sum_{l=0}^{L-1} \sqrt{\frac{a_l}{\lambda}} |l\rangle, \text{SELECT} = \sum_{l=0}^{L-1} |l\rangle \langle l| \otimes \mathbf{U}_l \quad (\text{D5})$$

and performing fixed-point oblivious amplification on the $|0\rangle^{\otimes \kappa}$ state [32, 65] after constructing the gate

$$(\text{PREP}^\dagger \otimes \mathbf{I}_N) \cdot \text{SELECT} \cdot (\text{PREP} \otimes \mathbf{I}_N) \quad (\text{D6})$$

Block-encoding then enables the construction of a unitary operator

$$\mathbf{Q} = \mathbf{U}_H \begin{pmatrix} \mathbf{I}_{N \times N} & \mathbf{0}_{N \times (2^\kappa - N)} \\ \mathbf{0}_{(2^\kappa - N) \times N} & -\mathbf{I}_{(2^\kappa - N) \times (2^\kappa - N)} \end{pmatrix} \quad (\text{D7})$$

called the *qubitized walk-operator* [66]. When the block-encoding is exact, \mathbf{Q} has eigenvalues equal to $e^{\pm i \cos^{-1}(E_k/\lambda)}$, where E_k are the eigenvalues of \mathbf{H} .

Appendix E: Quantum Chebyshev Phase Estimation

In this section, we summarize the method proposed in [29] to estimate the eigenvalues of our non-Hermitian Hamiltonian. We recall that this loss of hermiticity is due to the additional non-Hermitian differential operators (40) and (41) that arise from the transcorrelation transformation and our inability to perform a symmetrization procedure similar to what was done in section II C 1. This quantum algorithm is only applicable to square matrices with real eigenvalues, which we conjecture is the case for our Hamiltonian due to numerical experiments with exact diagonalization. The method can be extended to eigenvalues that are contained in an area of the complex plane, but for simplicity we will only consider square matrices with real eigenvalues in the interval $[-1; 1]$.

1. Preliminaries on Chebyshev Polynomials

Definition E.1 (Chebyshev Polynomials of the First and Second Kinds [67]).

- The ℓ th Chebyshev polynomial of the first kind $T_\ell : [-1; 1] \rightarrow [-1; 1]$ is defined as:

$$T_\ell(x) = \cos(\ell \arccos(x)) \quad (\text{E1})$$

with generating function

$$\sum_{\ell=0}^{\infty} T_\ell(x) y^\ell = \frac{1 - yx}{1 + y^2 - 2yx} \quad (\text{E2})$$

It is also convenient to define the rescaled Chebyshev polynomials of the first kind:

$$\tilde{T}_\ell(x) = \begin{cases} \frac{1}{2} T_0(x) & \text{if } \ell = 0 \\ T_\ell(x) & \text{if } \ell \geq 1 \end{cases} \quad (\text{E3})$$

with generating function

$$\sum_{\ell=0}^{\infty} \tilde{T}_\ell(x) y^\ell = \frac{1 - yx}{2(1 + y^2 - 2yx)} \quad (\text{E4})$$

- The ℓ th Chebyshev polynomial of the second kind $U_\ell : [-1; 1] \rightarrow [-1; 1]$ is defined as:

$$U_\ell(x) = \frac{\sin((\ell + 1) \arccos(x))}{\sin(\arccos(x))} \quad (\text{E5})$$

with generating function

$$\sum_{\ell=0}^{\infty} U_\ell(x) y^\ell = \frac{1}{1 + y^2 - 2yx} \quad (\text{E6})$$

2. The Algorithm

Definition E.2 (Chebyshev History State). Let \mathbf{H} be a square matrix with real eigenvalues and subnormalization constant $\alpha_H > \|\mathbf{H}\|_2$. Consider an v qubit register and an arbitrary state $|\psi\rangle$. The total system is said to form a Chebyshev history state of \mathbf{H} if it can be written as

$$\sum_{\ell=0}^{v-1} |\ell\rangle \otimes T_\ell\left(\frac{\mathbf{H}}{\alpha_H}\right) |\psi\rangle \quad (\text{E7})$$

up to a normalization constant, where T_ℓ is the ℓ th Chebyshev polynomial of the first kind as defined in (E1).

The reason for the name *history state* is the fact that the v qubits register $|\ell\rangle$ serves as a counter that indicates the order of the Chebyshev polynomial of \mathbf{H}/α_H that is applied on the state $|\psi\rangle$ in the sum. Suppose now that $|\psi\rangle$ is the eigenvector of \mathbf{H} corresponding to its ground state, ie $|\psi\rangle = |\psi_0\rangle$ such that $\mathbf{H}|\psi_0\rangle = E_0|\psi_0\rangle$. Then, the history state takes the form

$$\sum_{\ell=0}^{v-1} |\ell\rangle \otimes T_\ell\left(\frac{\mathbf{H}}{\alpha_H}\right) |\psi_0\rangle = \sum_{\ell=0}^{v-1} T_\ell\left(\frac{E_0}{\alpha_H}\right) |\ell\rangle \otimes |\psi_0\rangle = \sum_{\ell=0}^{v-1} \cos(2\pi\ell\phi) |\ell\rangle \otimes |\psi_0\rangle \quad (\text{E8})$$

where $\phi = \frac{1}{2\pi} \arccos \frac{E_0}{\alpha_H}$. We now neglect the $|\psi_0\rangle$ register, whose purpose was to phase-kickback the cosine term to the v qubit register, and apply a quantum Fourier transform:

$$QFT \sum_{\ell=0}^{v-1} \cos(2\pi\ell\phi) |\ell\rangle = \frac{1}{2\sqrt{v}} \sum_{\ell=0}^{v-1} \sum_{\ell'=0}^{v-1} \left(e^{2\pi i \ell'(\phi - \frac{\ell}{v})} + e^{-2\pi i \ell'(\phi + \frac{\ell}{v})} \right) |\ell\rangle \quad (\text{E9})$$

If we scale $\alpha_H > 2\|\mathbf{H}\|_2$, the authors show that, by measuring ℓ in the computational basis, we obtain an approximate of $v\phi$ with a success probability greater than $1/2$. More precisely, starting from a Chebyshev history state (E13), performing a QFT, and measuring in the computational basis gives a value ℓ satisfying

$$|cmod_1\left(\frac{\ell}{v} \pm \phi\right)| < \frac{v'}{v} \quad (\text{E10})$$

with probability at least 0.566 for $v' \geq 5$. Here, *cmod* refers to the centered modulus function defined as

$$cmod_q(x) = x - q \lfloor \frac{x + \frac{q}{2}}{q} \rfloor \quad (\text{E11})$$

The success probability can then be boosted to at least $1-p_f$ by repeating the procedure $\mathcal{O}(\log(1/p_f))$ times. However, one must first be able to generate Chebyshev history states.

Lemma E.1. Let \mathbf{H} be a square matrix with real eigenvalues and subnormalization constant $\alpha_H > \|\mathbf{H}\|_2$ and let $\mathbf{L}_v = \sum_{\ell=0}^{v-2} |\ell+1\rangle\langle\ell|$ be the $v \times v$ lower shift operator. The matrix version of the operator of the generating function for rescaled Chebyshev polynomials (E4)

$$G\left(\frac{\mathbf{H}}{\alpha_H}\right) = \sum_{\ell=0}^{v-1} \mathbf{L}_v^\ell \otimes \tilde{T}_\ell\left(\frac{\mathbf{H}}{\alpha_H}\right) \quad (\text{E12})$$

applied on the $|0\rangle \otimes |\psi\rangle$ state gives the rescaled Chebyshev history state

$$\sum_{\ell=1}^{v-1} |\ell\rangle \otimes \tilde{T}_\ell\left(\frac{\mathbf{H}}{\alpha_H}\right) |\psi\rangle \quad (\text{E13})$$

Proof. It is a straightforward application of the operator G , noticing that elevating the $v \times v$ lower shift operator to the ℓ th power gives

$$\mathbf{L}_v^\ell = \sum_{\ell'=0}^{v-1-\ell} |\ell+\ell'\rangle\langle\ell'| \quad (\text{E14})$$

□

In order to use the Chebyshev quantum phase estimation algorithm, we thus have to apply this operator to the zeroed v qubit register. To implement it as a gate on a quantum computer, we first define a padding of the matrix \mathbf{H}/α_H :

$$\begin{aligned} Pad\left(\frac{\mathbf{H}}{\alpha_H}\right) &= \mathbf{I}_v \otimes \mathbf{I} + \mathbf{L}_v^2 \otimes \mathbf{I} - 2\mathbf{L}_v \otimes \frac{\mathbf{H}}{\alpha_H} \\ &= \begin{pmatrix} \mathbf{I} & 0 & \dots & \dots & \dots & 0 \\ -2\mathbf{H}/\alpha_H & \mathbf{I} & \ddots & \ddots & \ddots & \vdots \\ \mathbf{I} & -2\mathbf{H}/\alpha_H & \mathbf{I} & \ddots & \ddots & \vdots \\ 0 & \mathbf{I} & -2\mathbf{H}/\alpha_H & \mathbf{I} & \ddots & \vdots \\ \vdots & \ddots & \ddots & \ddots & \ddots & \vdots \\ 0 & \dots & 0 & \mathbf{I} & -2\mathbf{H}/\alpha_H & \mathbf{I} \end{pmatrix} \end{aligned} \quad (\text{E15})$$

and use the following lemma.

Lemma E.2.

$$G\left(\frac{\mathbf{H}}{\alpha_H}\right) = Pad\left(\frac{\mathbf{H}}{\alpha_H}\right)^{-1} \cdot \left(\frac{\mathbf{I}_v - \mathbf{L}_v^2}{2} \otimes \mathbf{I} \right) \quad (\text{E16})$$

Proof. Inverting the right-hand side of (E15) and multiplying by $\frac{\mathbf{I}_v - \mathbf{L}_v^2}{2} \otimes \mathbf{I}$, we obtain the form of the generating function for the rescaled Chebyshev polynomials of (E4) with $x = \mathbf{I}_v \otimes \frac{\mathbf{H}}{\alpha_H}$ and $y = \mathbf{L}_v \otimes \mathbf{I}$. \square

Since finding the inverse of a matrix, let alone on a quantum computer, is a tedious task, we will get our Chebyshev history state by solving the linear system

$$Pad\left(\frac{\mathbf{H}}{\alpha_H}\right) |\Phi\rangle \otimes |\psi\rangle = \frac{|0\rangle - |2\rangle}{2} \otimes |\psi\rangle \quad (\text{E17})$$

for a state $|\Phi\rangle \in \mathcal{H}^{2^v}$. The right-hand side of the equation results from applying the operator $\frac{\mathbf{I}_v - \mathbf{L}_v^2}{2} \otimes \mathbf{I}$ to the $|0\rangle \otimes |\psi\rangle$ state. Many quantum linear system solvers have been proposed, but the authors propose to use the one described in [68]. The task of block-encoding the gate $Pad(\mathbf{H}/\alpha_H)$ and the lower shift matrix is one that will not be discussed in this work, as it has been extensively elaborated on in [29].

Algorithm: Quantum Chebyshev Phase Estimation

1. Construct a block encoding of the target matrix \mathbf{H} and the lower shift matrix \mathbf{L}_v .
2. Use \mathbf{L}_v and \mathbf{H} to form the $Pad(\mathbf{H}/\alpha_H)$ gate according to equation (E15).
3. Prepare the v qubit register in the state $\frac{|0\rangle - |2\rangle}{2}$.
4. Invoke the quantum linear system solver to solve equation (E17) for $|\Phi\rangle$.
5. Perform the quantum Fourier transform and measure in the computational basis.
6. Boost the success probability using median amplification.

The general theorem for the Chebyshev phase estimation IV.1 takes into account (i) the error from the quantum linear system solver, (ii) the distance between the prepared state $|\psi\rangle$ and the true ground state eigenstate $|\psi_0\rangle$ and (iii) the fact that we are approximating a rescaled Chebyshev history state (E.1) to a normal one (E13). Finally, for preparing an initial state that is close to the true ground state, the authors introduce an algorithm for preparing the ground state of a non-Hermitian matrix using *Quantum EigenValue Transformation* (QEVT). It mainly consists of forming a more general Chebyshev state than the one in (E13), which requires the construction of an extended $Pad(A)$ matrix.